Materials Horizons

ROYAL SOCIETY OF CHEMISTRY

COMMUNICATION

View Article Online
View Journal | View Issue

Cite this: *Mater. Horiz.*, 2025, 12, 5855

Received 5th February 2025,
Accepted 12th May 2025

DOI: 10.1039/d5mh00214a

rsc.li/materials-horizons

2D MoS_2/Cu_2O on 3D mesoporous silica as visible-NIR nanophotocatalysts for environmental and biomedical applications†

Gubakhanim Shahnazarova,‡[ab] Jessica C. Ramirez,‡[ab] Nour Al Hoda Al Bast,[ab] Jordi Fraxedas,[a] Aritz Lafuente,[ab] Cristina Vaca,[bc] Marianna Sledzinska,[a] Valentin Novikov,[de] Carme Nogues,[b] Josep Nogues,[af] Albert Serra,[eg] Borja Sepulveda*[c] and Maria J. Esplandiu*[a]

Nanostructures based on transition metal dichalcogenides have attracted considerable attention due to their tunable optoelectronic properties and large surface areas, showing a great potential as photocatalysts. Here, a novel supported structure based on 2D-MoS_2/Cu_2O nanoflakes grown on 3D mesoporous silica templates fabricated by a combination of solvothermal synthesis and e-beam deposition methods is presented. The synthesized MoS_2 nanoflakes exhibited a combination of trigonal-prismatic 2H and distorted-trigonal 1T′ phases, which contributed to a high density of active catalytic sites, facilitating efficient photogenerated charge transfer to analytes at the liquid interface. The deposition of Cu on the MoS_2 nanoflakes enabled the formation of a semiconducting MoS_2/Cu_2O heterostructure with greatly enhanced photocatalytic activity. The supported MoS_2/Cu_2O nanoflakes showed excellent stability and an efficient generation of reactive oxygen species (ROS) with white and near infrared (NIR) light. The photocatalytic potential of the MoS_2/Cu_2O nanoflakes was established by the nearly complete degradation and mineralization of two organic pollutants (the antibiotic tetracycline and the biotoxin anatoxin-A) under low intensity white light, using ultralow catalyst concentration (*ca.* 4 μg mL^{-1}). In addition, the use of MoS_2/Cu_2O nanostructures as photodynamic agents under low intensity NIR light was demonstrated. The NIR illuminated MoS_2/Cu_2O nanoflakes, placed at a distance of 120 μm from cultured cancer cells, enabled the complete elimination of cells *via* apoptosis, despite the large separation between them. These results underline the high photocatalytic activity of the supported MoS_2/Cu_2O nanoflakes to produce ROS with visible and NIR light, thus highlighting their suitability for environmental remediation and biomedical applications.

New concepts

In this manuscript, we introduce a novel and highly reactive photocatalytic platform with dual functionality for both environmental remediation and biomedical applications, achieved by fabricating a hybrid 2D MoS_2/Cu_2O nanoflake structure supported on mesoporous silica nanoparticles. The system combines the unique 2H/1T′ phase of MoS_2 with Cu_2O to form a synergistic heterostructure that significantly enhances light absorption, charge separation, and catalytic activity. The MoS_2 expanded 2D stacking layers and abundant active sites notably boost photocatalytic performance, enabling efficient degradation and mineralization of organic pollutants such as tetracycline and anatoxin-A. Remarkably, this system outperforms previous studies by achieving high catalytic efficiency at ultra-low concentrations (~4 μg mL^{-1}), reducing the need for large catalyst amounts. Furthermore, the platform demonstrates very good recyclability and minimal secondary pollution, making it a highly sustainable solution for environmental applications. Additionally, we highlight its substantial potential in biomedical applications, where it effectively generates reactive oxygen species under low-intensity NIR light for photodynamic therapy in cancer treatments, positioning it as a promising candidate for use in the first biological window.

1. Introduction

Within photocatalytic materials, 2D transition metal dichalcogenides (TMDs), particularly MoS_2, have attracted wide attention due to their tunable bandgap, favorable band alignment for added-value chemical reactions, earth abundance, and cost-effectiveness.[1] MoS_2 exhibits a polyphasic nature, featuring a

[a] *Catalan Institute of Nanoscience and Nanotechnology (ICN2), CSIC and BIST, Campus UAB, Bellaterra, E-08193, Barcelona, Spain. E-mail: mariajose.esplandiu@icn2.cat*
[b] *Universitat Autònoma de Barcelona, 08193 Cerdanyola del Vallès, Barcelona, Spain*
[c] *Instituto de Microelectrónica de Barcelona (IMB-CNM, CSIC), Barcelona, 08193, Spain. E-mail: borja.sepulveda@csic.es*
[d] *Departament de Química Inorgànica i Orgànica, Secció Química Inorgànica, Universitat de Barcelona, Martí i Franquès, 1, E-08028, Barcelona, Catalonia, Spain*
[e] *Institute of Nanoscience and Nanotechnology (IN2UB), Universitat de Barcelona, Barcelona, Catalonia, Spain*
[f] *ICREA, Pg. Lluís Companys 23, 08010 Barcelona, Spain*
[g] *Grup d'Electrodeposició de Capes Primes i Nanoestructures (GE-CPN), Departament de Ciència de Materials i Química Física, Universitat de Barcelona, Martí i Franquès, 1, E-08028, Barcelona, Catalonia, Spain*

† Electronic supplementary information (ESI) available. See DOI: https://doi.org/10.1039/d5mh00214a

‡ Gubakhanim Shahnazarova and Jessica C. Ramirez contributed equally to this work

stable hexagonal 2H phase and metastable 1T or distorted 1T′ octahedral phases. These phases arise from the formation of different coordination bonds between Mo and S atoms, which significantly impact the electronic, optical, and chemical properties of MoS_2.[2,3] The bulk 2H phase of MoS_2 holds semiconducting properties, with a bandgap that varies with the number of layers, enabling valuable applications in optoelectronics and photonics.[1] In contrast, the 1T phase is metallic, while the distorted octahedral 1T′ phase is a very small-bandgap semiconductor.[4] These 1T phases show great potential in energy conversion and storage, (photo)catalysis, biosensing, and photothermal therapies, due to their reduced charge transfer resistance.[5–8]

The synthesis conditions significantly influence the prevalence and coexistence of the different MoS_2 phases. For example, in liquid synthetic routes, factors such as ion intercalation, charge injection, strain, pH, and temperature play a critical role in determining the structural phase of MoS_2 and their ultimate properties.[9–11] Reported studies have shown that combinations of different MoS_2 phases are highly efficient catalysts, particularly for hydrogen evolution reactions and wastewater remediation.[12–16] The direct bandgap of 2H-MoS_2 enables efficient photon absorption, which can be exploited in photocatalytic reactions to produce reactive oxygen species (ROS) through the activation of oxygen.[17] Furthermore, the coexistence of 2H and 1T phases can enhance charge separation, as the higher conductivity of the 1T and 1T′ phases facilitates efficient photocarrier transfer, reducing recombination and boosting photocatalytic efficiency.[18–21] Additionally, the 1T phase has a higher absorption coefficient in the visible light range compared to the 2H phase, and a mixed-phase structure broadens the range of absorbed wavelengths, improving overall photocatalytic activity.[22]

Edge sites in MoS_2 are also key for photocatalysis.[23,24] The 2H phase of MoS_2 primarily exhibits active sites at the stacked layer edges, and efforts have focused on increasing their density at the liquid/MoS_2 interface. While the growth of vertically aligned stacked layers of MoS_2 offers a promising strategy to increase the edge density and catalytic activity,[23,25] other approaches, such as creating mixed-phase structures or introducing defects and vacancies,[26,27] can also achieve high edge density and improve the overall performance. The coexistence of the 1T phase, which often contains more abundant active sites, not only at the edges but also at structural defects such as vacancies and dislocations, provides a practical alternative. These additional sites can enhance photocatalytic reactions by facilitating the adsorption of reactants and boosting reaction rates. Moreover, the photocatalytic activity of MoS_2 can be further enhanced by forming heterojunctions with suitable semiconductors and metallic structures.[22,28–32] Therefore, exploring new alternatives to promote these different features is essential for optimizing photocatalytic efficiency.

Beyond photocatalytic performance, the recovery of the catalytic structures from solution after pollutant degradation remains a significant concern. This process is often complex, costly, and may potentially cause secondary pollution when used as dispersed heterogeneous catalysts. Growing MoS_2 on a solid support may alleviate these issues[33–35] but its 2D nature could significantly decrease the number of active sites for catalytic reactions. Thus, new strategies are needed to develop supported MoS_2 structures maximizing surface area and active sites while achieving a high degree of mineralization.

Here, with the aim of achieving highly reactive 2D MoS_2 on a substrate, we fabricated MoS_2 nanostructures on supported mesoporous silica nanoparticles by a cost-effective solvothermal process with an ammonium-based precursor. The mesoporous template transfers its high surface area characteristics to MoS_2 during growth and also promoting the enrichment of MoS_2 edge and defect catalytic sites. Additionally, a thin Cu_2O layer was deposited on the grown MoS_2, forming a heterojunction, to significantly enhance the photocatalytic reaction. The optimized MoS_2/Cu_2O nanoflakes exhibited a remarkable photocatalytic performance in a wide pH range, being capable of degrading and mineralizing organic pollutants and biotoxins with white light. In addition, the MoS_2/Cu_2O nanoflakes exhibited very high efficacy to kill cancer cells by illumination with low-intensity near-infrared light in the first biological window (660–808 nm). Therefore, the MoS_2/Cu_2O heterojunction nanoflakes on the 3D mesoporous supports could be appealing for both environmental remediation and therapeutic applications.

2. Results and discussions

2.1. Fabrication and physicochemical characterization

The fabrication process of the supported MoS_2/Cu_2O nanoflakes followed four steps (Fig. 1): (i) fabrication and self-assembly of the mesoporous silica nanoparticles on a solid support,[36] (ii) silanization of the silica surface with (3-aminopropyl)Triethoxysilane (APTES) to improve interaction with the growing MoS_2, (iii) solvothermal growth of the MoS_2 nanoflakes and (iv) copper deposition by e-beam deposition. As comparison, we also fabricated MoS_2 monolayer flakes by chemical vapor deposition (CVD).

The scanning electron microscopy (SEM) image in Fig. 2a shows that the MoS_2 flakes form a high density and uniform 3D network on the mesoporous silica particles. The low-resolution transmission electron microscopy (TEM) image confirms the 2D character of the MoS_2 flakes (Fig. 2b). We also obtained high-resolution TEM (HRTEM) images that reveal distinct atomic arrangements, which can be attributed to the 2H and 1T′ crystallographic phases of MoS_2 (Fig. 2c and d). However, high resolution imaging remains challenging due to the mesoporous and amorphous nature of the silica support, which causes scattering and contrast loss, significantly hindering direct phase identification. Interestingly, we also observe a significantly increased interlayer spacing in MoS_2 of approximately 0.8–1 nm (Fig. 2e and f), markedly larger than the typical 0.62 nm spacing reported for 2H MoS_2.[37–39] Note that the expanded spacing, often observed in 1T structures, is beneficial for enhancing catalytic capabilities.[14,40,41] In addition, electron energy loss spectroscopy (EELS) and energy dispersive X-ray spectroscopy (EDS) mappings qualitatively reveal the uniform

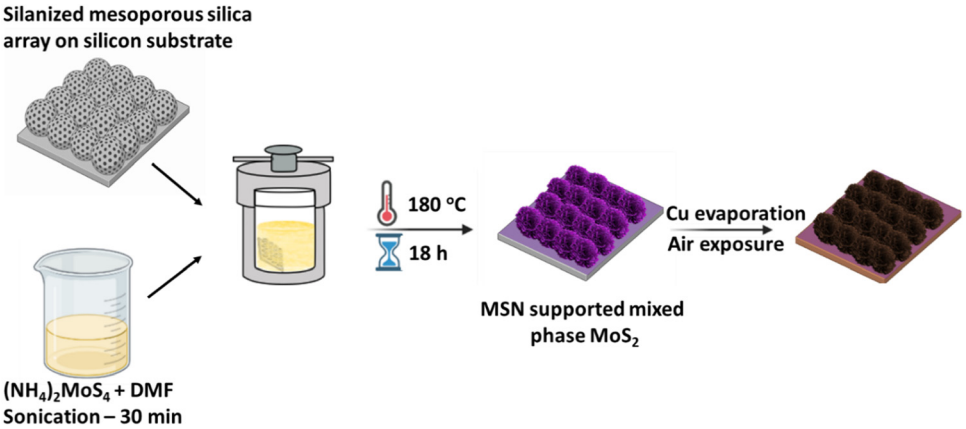

Fig. 1 Fabrication process of the photocatalyst. Schematic representation of the fabrication process for MoS_2/Cu_2O nanoflakes, achieved through a combination of solvothermal synthesis and metal evaporation (DMF: dimethylformamide; MSN: mesoporous silica nanoparticles).

distribution of the Cu, Mo and S elements and the absence of contaminants (Fig. S1, ESI†).

To determine their crystallographic and electronic structures, the samples were analyzed by UV-Vis spectroscopy, photoluminescence, Raman spectroscopy, XRD and XPS. The results were compared to CVD-grown MoS_2 flakes, which are known to exhibit the more stable 2H or 1H phases. The UV-Vis spectra of the CVD MoS_2 exhibited the expected three characteristic absorption peaks, appearing at approximately 667 nm, 614 nm and 440 nm (Fig. 3), which correspond to the generation of the A, B, and C excitons, respectively.[42] These peaks are typical for the 2D semiconducting 2H/1H phases. In contrast, the solvothermal MoS_2 showed no distinct peaks; instead, it evidenced an increased light absorbance across the entire inspected wavelength range (Fig. 3). The broader absorbance is beneficial for the photocatalytic performance, as it allows solvothermal MoS_2 to harness a wider spectrum of light for enhanced catalytic activity.[22] Moreover, the CVD MoS_2 exhibited strong photoluminescence as a result of direct band gap excitations at the K point of the Brillouin zone, whereas the solvothermal MoS_2 did not show any photoluminescence, which could be due to the presence of phases with very small bandgap or a more metallic nature (Fig. 3b). The mixed 2H-1T phase can quench photoluminescence through non-radiative pathways, such as charge transfer between the semiconducting 2H phase and the more conductive 1T phase. This charge transfer is highly beneficial for photocatalysis, as it promotes the injection of carriers into the electrolytic medium.

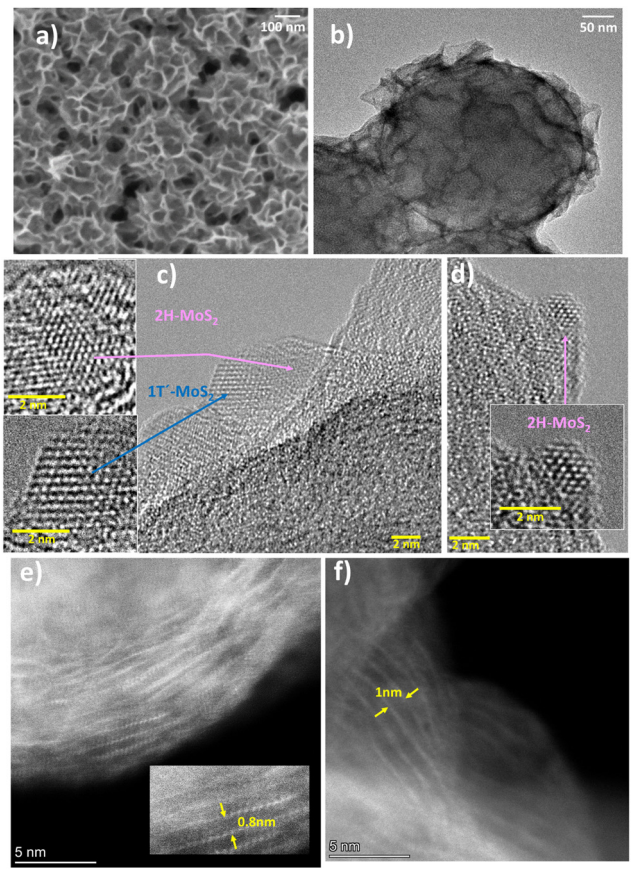

Fig. 2 Electron microscopy characterization. (a) SEM and (b) TEM images of the solvothermally grown MoS_2/Cu_2O nanoflakes. (c) and (d) HRTEM images of solvothermally synthesized MoS_2 on silica, exhibiting distinct crystal structures, with the insets showing zoomed regions. (e) and (f) Scanning TEM (STEM) images of MoS_2 displaying the interlayer distances.

To shed more light on the electronic structure, Raman spectroscopy was also carried out on the CVD and solvothermal MoS_2. As show in Fig. 3c, the CVD MoS_2 contained only the two main peaks associated with the 2H phase: the E_{2g} mode at 384 cm^{-1}, and the A_{1g} mode at 410.15 cm^{-1}. In contrast, the Raman spectrum of the solvothermal MoS_2 revealed multiple peaks, indicative of a more complex phase composition (Fig. 3c). The J_1 peak (143.6 cm^{-1}) illustrates the presence of a quite defective phase, that is related with a T′ phase.[43] Additionally, the J_2 (223.6 cm^{-1}) and J_3 (350.6 cm^{-1}) modes, characteristic of the T phases, illustrate the shifting of S atoms with respect to Mo atoms. Furthermore, the two typical E_{2g} and A_{1g} Raman modes, although slightly shifted, implied that a 2H phase is also present in the solvothermal sample. Noticeable shifts and broadening of the E_2g^1 and A_1g Raman modes of 2H-MoS_2 have been also reported in literature and attributed to

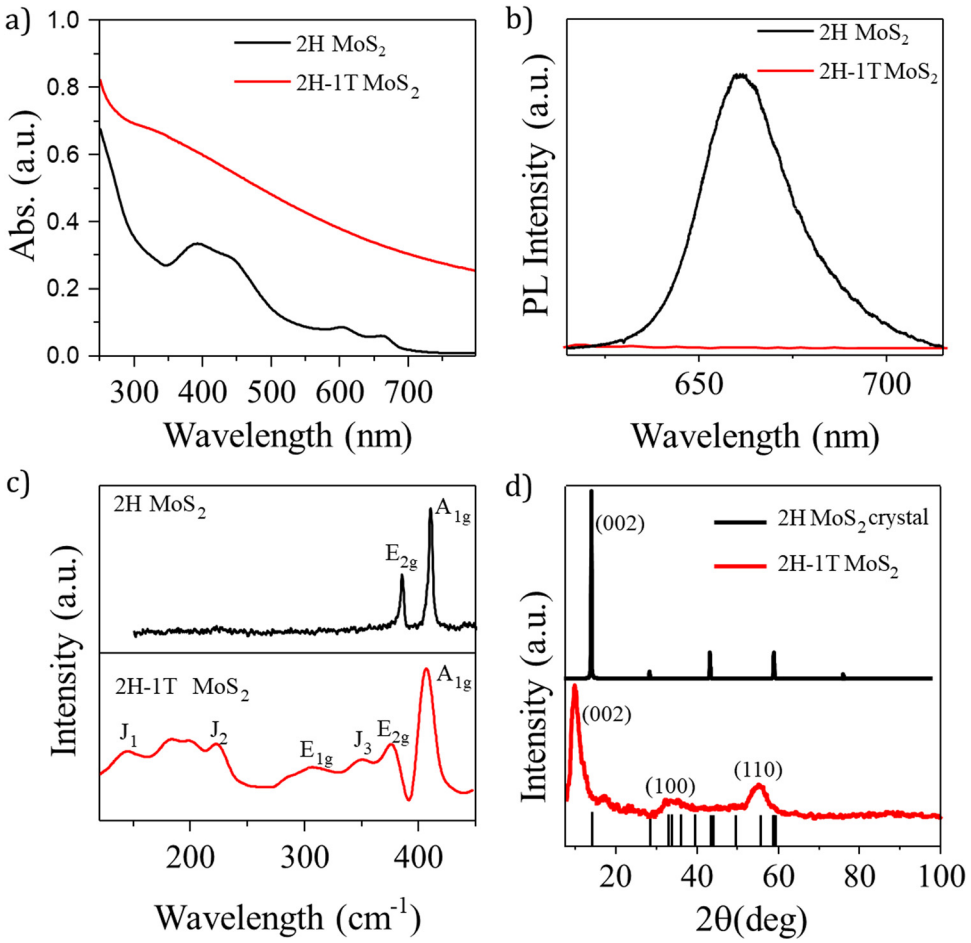

Fig. 3 Spectroscopic and structural characterization of MoS_2 samples grown by CVD and by solvothermal processes. (a) UV-VIS absorption (Abs) spectra, (b) photoluminescence (PL) spectra, (c) Raman spectra and (d) XRD patterns of the solvothermally grown sample. In panel (d) a bulk 2H-MoS_2 crystal, and the reference peak positions for 2H-MoS_2 from JCPDS Card No. 37-1492 have been included for reference.

structural disorder, low crystallinity, strain effects, and the coexistence of 2H and 1T phases.[44–47]

The XRD pattern of solvothermally synthesized MoS_2 is shown alongside the diffraction pattern of bulk 2H-MoS_2 and the reference peak positions from the JCPDS card for 2H-MoS_2. The latter data were included due to the difficulty in obtaining intense diffraction signals from the monolayer CVD-grown 2H-MoS_2 (Fig. 3d). The solvothermal sample exhibited relatively poor crystallinity. Moreover, a diffraction peak was observed at 9.5°, corresponding to the (002) plane of the MoS_2 crystal structure, which represents the interlayer spacing between stacked MoS_2 layers.[48,49] This peak is shifted to a lower angle, compared to the bulk MoS_2 and JCPDS reference (~14.4°), suggesting a larger interlayer distance. The estimated interlayer distance using Bragg's law was approximately 0.93 nm, in concordance with the TEM images which showed experimental values typically ranging between 0.8 and 1.0 nm. This is significantly larger than the interlayer distance of around 0.62 nm for the (002) plane of bulk 2H-MoS_2, with an XRD peak at ~14.4°. These XRD findings align with the TEM analyses and point to the incorporation of defects, increased structural disorder, and possible intercalation of ammonium ions.

To gain insights into the phases appearing in the solvothermally grown MoS_2, Fig. 4 presents comparative high-resolution XPS spectra of the Mo3d/S2s lines (left) and the S2p lines (right) for (a) a mechanically exfoliated MoS_2 natural crystal, (b) CVD-grown MoS_2, and (c) solvothermal MoS_2, respectively.

The deconvolution of the Mo3d lines in Fig. 4a and b (left) exhibit a main contribution of the Mo3d doublets (blue lines) centered at 229.5–229.6 eV ($Mo3d_{5/2}$), a minor contribution (green lines) centered at 232.6–232.7 eV and a single S2s peak at 226.7–226.9 eV (magenta lines). The S2p lines in Fig. 4a and b (right) show a single doublet (blue lines), with the $S2p_{3/2}$ lines centered at 162.4–162.5 eV and with a full width at half maximum (FWHM) of 0.7 eV.[50] The 229.5–229.6 and 162.4–162.5eV features are characteristic of n-type 2H MoS_2 (Mo^{4+})[51–53] and the 232.6–232.7 eV is assigned to MoO_3 (Mo^{6+}),[54] respectively. This is further evidenced by the position of the valence band maximum (VBM) that is located at 1.3 eV below the Fermi level of the system [see inset in Fig. 4(a)]. Such VBM value is nearly the full indirect band gap of bulk MoS_2, indicating that the Fermi level should be very close to the conduction band maximum.[52]

In the case of the CVD grown MoS_2, an extra small contribution at 230.5 (Mo3d) is observed (wine-colored lines). The origin of the

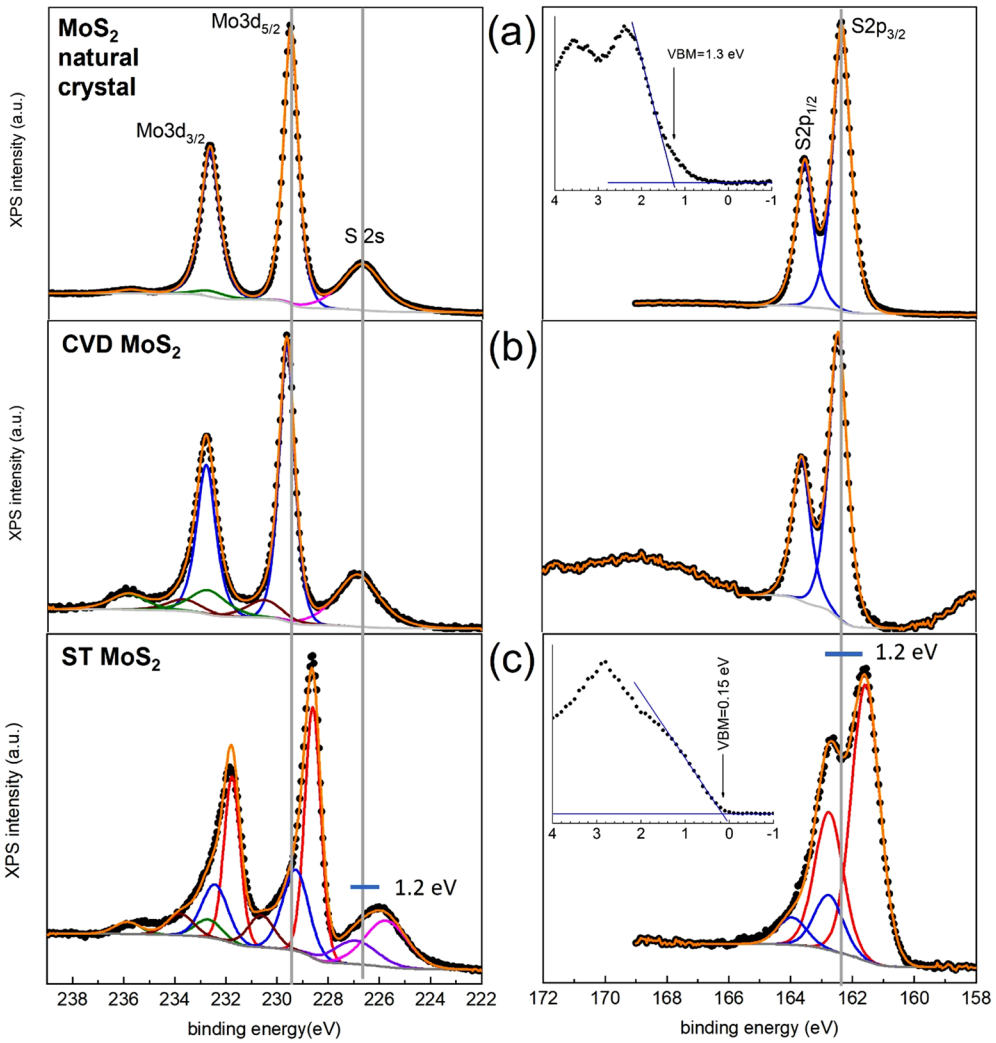

Fig. 4 XPS analysis of MoS_2 samples. XPS spectra of the Mo3d/S2s lines (left) and of the S2p lines (right) for (a) mechanically exfoliated MoS_2 natural crystal, (b) CVD grown MoS_2, and (c) MoS_2 prepared by solvothermal (ST) methods. Least-squares fits of the experimental data (full black dots) are included (see details in Materials and methods section). Continuous gray straight lines are shown to guide the eye. The insets of (a) and (b) correspond to valence band, where the valence band maximum (VBM) values are also indicated.

230.5 eV might be assigned to MoO_2 (Mo^{4+})[55] but certainly not to Mo_2S_5[56] since we observe single S2s and S2p double lines.

The convolution of the spectra corresponding to the solvothermal MoS_2 sample is more complex. From Fig. 4c (left) we obtain two S2s contributions (magenta and violet lines) at 225.7 and 226.9 eV, respectively (1.2 eV shift) and four contributions to the Mo3d lines with the corresponding $Mo3d_{5/2}$ lines centered at 228.6 (red line), 229.3 (blue line), 230.6 (wine-colored line) and 232.7 eV (green line), respectively. No feature at about 231.4 eV is observed, characteristic of MoS_3, so that the presence of this component can be safely ruled out.[57] Additionally, the feature at 230.5 eV, identified in the CVD sample, is also present. In the inset we observe that the VBM is located at 0.15 eV. As can be seen in Fig. 4c (right), the region between 166 and 158 eV binding energies is satisfactorily deconvoluted with two doublets, with the $S2p_{3/2}$ lines centered at 161.6 (red line) and 162.8 eV (blue line), respectively, with a 1.1 eV FWHM. The shift between both components is 1.2 eV.

No hint of oxidation states lower than 4^+, *e.g.*, Mo^{3+}, were observed. Recently, a critical review on the experimental characterization of the MoS_2 1T phases has pointed out the presence of Mo^{3+} species.[10] In the case of XPS experiments this is based on the observation of binding energies of the $Mo3d_{5/2}$ line of about 228 eV, but when dealing with defective semiconductors band bending can shift the binding energies without the relevant presence of lower oxidation states.[50,58,59]

Fig. 4c evidences the presence of two different MoS_2 phases in the solvothermal samples. We identify n-type 2H MoS_2 (blue lines), with the $Mo3d_{5/2}$ and $S2p_{3/2}$ peaks located at 229.3 and 162.8 eV, respectively, and a second phase (red lines) whose binding energies are rigidly shifted by about 1.2 eV towards lower energies, a value that approaches the full indirect band gap of MoS_2. The comparison of the FWHM of the S2p line corresponding to the solvothermal sample (above 1 eV), natural crystal and CVD samples (0.7 eV) evidence considerable disorder in the solvothermal sample due to the presence of defects, which can induce the pinning of the Fermi

level and thus the band bending.[60,61] All these features indicate that the proposed 1T phase could be either a defective p-type 2H-MoS_2 or a defective small-gap octahedral phase. Previous UV-visible absorbance measurements, in which the absorption bands of 2H-MoS_2 were smeared out, also indicate that the spectrum is dominated by octahedral T phases, which have a more metallic character, rather than a p-type 2H MoS_2. This is supported by the lack of photoluminescence signals on the solvothermal samples, indicating again that the overall performance is dominated by a more metallic character. However, a pure metallic phase is ruled out since the VBM lies below the Fermi level of the system by 0.15 eV. Such finding discourages the presence of the pure metallic T phase and is more consistent with the presence of the distorted T′ phase, which exhibits small bandgaps and is more prone to defects, doping and lattice deformation inducing band shifting and band bending.[4]

Finally, the XPS measurements were performed on the solvothermal MoS_2 samples after Cu deposition (Fig. S2, ESI†). The binding energy and shape of the $Cu2p_{3/2}$ component (932.3 eV) and the shape of the Cu LMM line, which exhibits a prominent maximum at a kinetic energy of 917.1 eV, are indicative of +1 oxidation state for copper,[62] thereby confirming the formation of the MoS_2/Cu_2O heterostructure.

2.2. Photocatalytic degradation of organic pollutants

To determine the photocatalytic efficiency of the solvothermally grown supported MoS_2 and MoS_2/Cu_2O samples, we investigated first their ability to degrade tetracycline (TC), a widely recognized antibiotic pollutant in water. The degradation of this benchmark pollutant was monitored at pH = 6 and pH = 8. The changes of the TC absorbance were acquired during 180 min of irradiation with visible light (Fig. 5a). The degree of TC degradation of the bare solvothermal MoS_2 nanoflakes was 33.1% and 43.9% at pH = 6 and pH = 8, respectively. Remarkably, the deposition of a thin 3 nm copper layer on the MoS_2 significantly raised the degradation rate of TC to 90% and 92% at pH = 6 and pH = 8, respectively, indicating its excellent catalytic performance (Fig. 5b).

The photodegradation kinetics (Fig. 5c) shows that the addition of Cu increased the rate constant 5.95 and 4.05-fold (from 0.002 min^{-1} to 0.013 min^{-1} and from 0.0034 min^{-1} to 0.014 min^{-1}) with respect to the bare MoS_2 at pH 6 and pH 8, respectively (Fig. 5d). Notably, only 73 μg of catalyst was used in 18 mL of TC in order to completely remove TC in 180 min, equivalent to a concentration of 0.004 g L^{-1}. Various MoS_2-based systems have been studied for TC degradation, but to our knowledge, none of them have used such a minute photocatalyst amount in a time frame scale of 100–180 minutes for degrading 5–10 mg L^{-1} of TC.[63–80] For a better comparison with previous studies, the mass-normalized kinetic constant was calculated ($k_N = k/m_{cat}$). The corresponding k_N values for TC at pH 6 and pH 8 using the MoS_2/Cu_2O catalyst were 178 min^{-1} g^{-1} and 192 min^{-1} g^{-1}, respectively. Table S1 in the

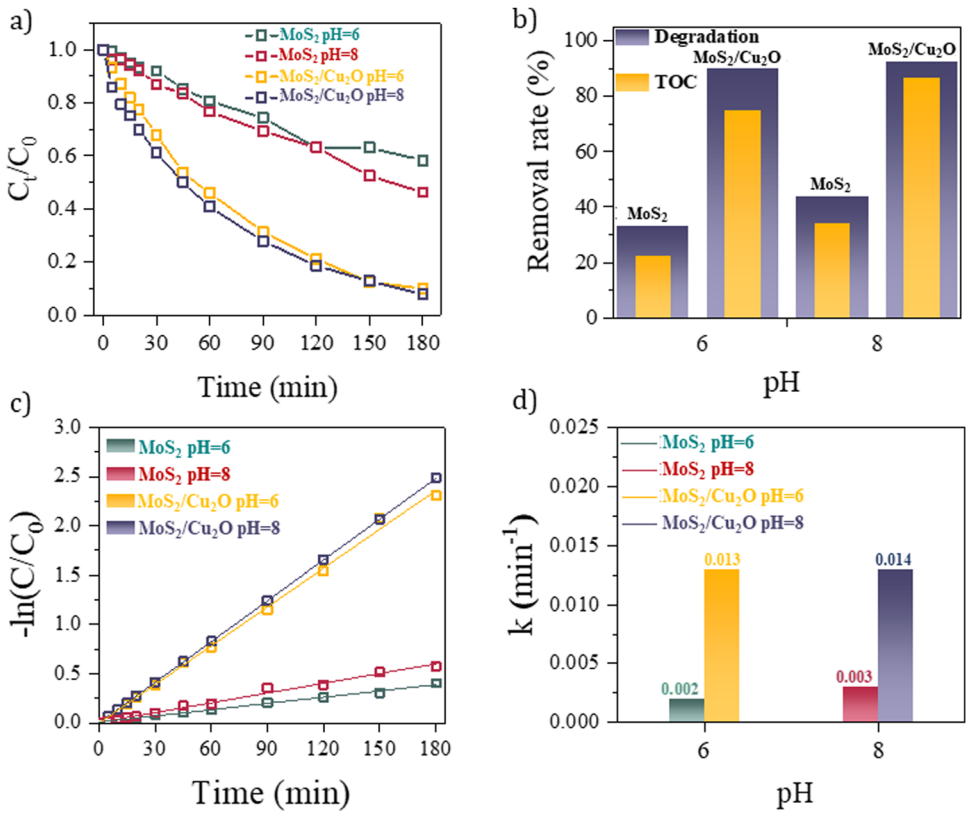

Fig. 5 TC degradation in the presence of solvothermal MoS_2 with/without Cu_2O at different pHs. (a) Variation of the TC concentration *versus* time. (b) Degradation and TOC removal percentage. (c) Reduction of the TC concentration over time in logarithmic scale, (d) obtained reaction rate (k) values.

ESI† provides a detailed comparison of degradation conditions reported for other studies. The table also includes studies conducted at higher TC concentrations,[81–96] studies achieving shorter degradation times,[20,28,86,97,98] and studies employing additional activation strategies such as H_2O_2/Fe^{2+} (photo-Fenton), PMS/PDS activation, or sonophotocatalysis.[99–104] However, most of these studies involve significantly larger catalyst amounts. Only very few studies report the use of small catalyst amounts (0.01 g L^{-1} and 0.017 g L^{-1}) achieving maximum k_N of 14 and 106 min^{-1} g^{-1}, respectively.[18,105,106] The rest use catalyst amounts equal to or greater than 0.1 g L^{-1} with k_N below 11 except for a system using Ag_3PO_4/MoS_2, where 0.2 g L^{-1} of catalyst achieved a k_N of 52 min^{-1} g^{-1}.[28]

Moreover, the MoS_2/Cu_2O system achieved a high total organic carbon (TOC) removal rate of 74.6% and 86.2% at pH = 6 and pH = 8 respectively, which was nearly 3-fold higher than the rate obtained with the bare MoS_2 system (22.6% at pH = 6, 33.8% at pH = 8) (Fig. 5b). It is important to emphasize that the mineralization efficiency is considerably large considering the results reported in the literature (Table S1, ESI†).[64,66,107–111]

Furthermore, to clarify the individual contributions of the photocatalyst components, additional experiments on TC degradation in the presence of silica/Cu_2O under dark and illuminated conditions were conducted, confirming the limited activity of the Cu_2O system alone. Additionally, control experiments using only the supported mesoporous silica showed that it did not promote TC adsorption under the working pH conditions, nor did it have any impact under light illumination (Fig. S3, ESI†)

To determine the reactive oxygen species (ROS) responsible of the photocatalytic degradation and mineralization of the organic pollutant, ROS quenching experiments targeting $^{\bullet}OH$, $^{\bullet}O_2^-$ and holes (h^+) were performed. We used 1 mM *p*-benzoquinone (*p*-BQ) as quencher of $^{\bullet}O_2^-$, 1 mM isopropanol (IPA) as quencher of $^{\bullet}OH$, and 1 mM triethanolamine (TEA) as quencher of h^+. Fig. 6a shows that the TC removal efficiency was significantly affected by IPA and *p*-BQ after 180 min. At pH = 8, only 16.3% and 34.5% TC was degraded in the presence of IPA and *p*-BQ, respectively. Similarly, in the presence of IPA and *p*-BQ, the nanoflakes decomposed 23.1% and 21.2% of TC at pH = 6, respectively. In contrast, when TEA was added, the removal rate was of 81.5% and 72.3% at pH = 6 and pH = 8, respectively, thus suggesting that $^{\bullet}OH$ and $^{\bullet}O_2^-$ were the main active species for TC removal.

Electron paramagnetic resonance (EPR) experiments were performed, and the formation of hydroxyl radicals ($^{\bullet}OH$) was successfully detected, although complex responses mediated by DMPO (5,5-dimethyl-1-pyrroline *N*-oxide), the ROS trapping agent, were observed. Hydroxyl radical generation was detected in all systems, silica/Cu_2O, silica/MoS_2, and silica/MoS_2/Cu_2O, even under ambient light conditions, as indicated by the formation of the DMPO–OH adduct. In addition to this signal, other spin-adducts were identified and are attributed to interactions between DMPO and trace metal ions present either in the solution or at the surface of the photocatalyst. Such interfering reactions hinder the reliable monitoring of reactive oxygen species generation with increasing light intensity; an effect more pronounced in systems containing copper-based components. This interference with radical detection using DMPO has been previously reported in the literature.[112] Notably, in the silica/MoS_2 system, despite the presence of secondary spin-adducts, a clear, consistent, and reproducible increase in the DMPO–OH signal was observed as light intensity increased. This behavior confirms the photogeneration of hydroxyl radicals in the current experimental conditions. A detailed description of the EPR measurements is provided in the ESI.† In contrast, the detection of $^{\bullet}O_2^-$ *via* EPR was unsuccessful, despite evidence from chemical quenching experiments using selective scavengers. Under the current experimental conditions, and in the presence of metal-based interferents that readily react with DMPO, the trapping of superoxide anions remains challenging. It is likely that the detected hydroxyl radicals could have resulted in part from the rapid interconversion of superoxide anions through secondary redox processes.

Evaluating reusability and stability is crucial for commercial wastewater treatment. Therefore, we performed several consecutive TC removal experiments at pH 6 and pH 8. Fig. 6b

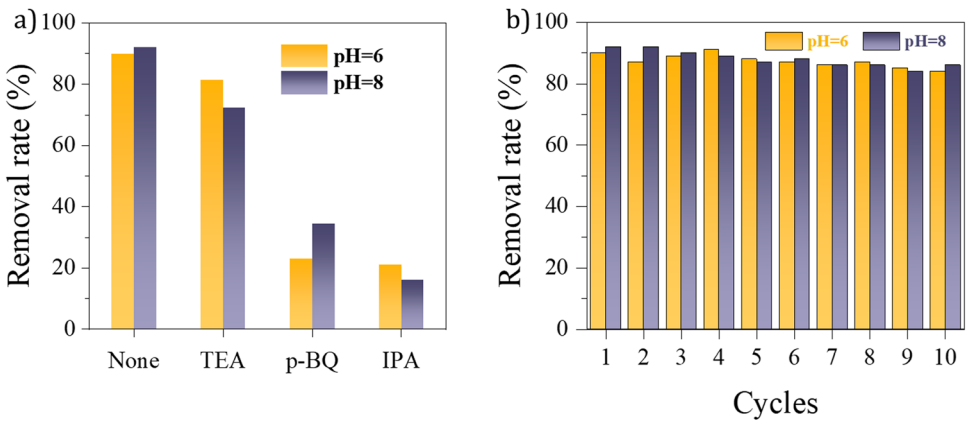

Fig. 6 ROS quenching and catalyst regeneration. (a) ROS quenching experiments in the presence of *p*-BQ, IPA and TEA. (b) Regeneration cycles of the catalyst.

revealed that the photocatalytic activity of MoS_2/Cu_2O nanoflakes was nearly unchanged even after 10 cycles both at pH = 6 and pH = 8.

Moreover, no morphological changes were observed by SEM for the silica/ST MoS_2/Cu_2O photocatalyst after multiple degradation cycles. However, to gain deeper insights into the impact of reusability, we also used spectroscopic techniques such as XPS and Raman spectroscopy, which are more sensitive to subtle structural and chemical changes (Fig. S9, ESI†). Raman spectroscopy confirmed that the overall phase composition remained largely stable, showing almost no changes after repeated use (Fig. S9, ESI†). Complementary XPS analysis supported this observation, revealing only very subtle variations in the Mo signals after extended cycling (specifically beyond eight degradation cycles) and notably, no increase in molybdenum oxide formation was detected. A very slight increase in the 2H-MoS_2 phase was detected. Importantly, the Cu_2O component consistently retained its +1 oxidation state throughout the degradation tests, which we believe is a consequence of the charge transfer pathway, as discussed later on. In summary, these results confirm that the MoS_2/Cu_2O nanoflakes could be a potential candidate for commercial wastewater treatment.

To prove the potential of the MoS_2/Cu_2O nanoflakes for complex environmental applications, we analyzed the removal of the cyanobacteria anatoxin-A under white light irradiation. Currently, the excessive reproduction and accumulation of cyanobacteria and the toxins they produce pose a growing challenge to the water industry.[113,114] In particular, anatoxin-A is one of the potent alkaloid neurotoxins produced by cyanobacteria globally.[113] Photocatalytic degradation using optimized materials presents a promising and cost-effective approach for fostering anatoxin-A breakdown. Some wider band-gap photocatalysts have already demonstrated significant performance in degrading anatoxin-A.[115,116] However, the potential of low-band-gap heterostructures based on transition metal dichalcogenides for this purpose remains largely unexplored.

We analyzed the anatoxin-A removal (initial concentration of 20 ppm) by the supported MoS_2/Cu_2O nanoflakes under white LED irradiation (52×10^{-3} W cm^{-2}). Fig. 7a shows the anatoxin-A chromatograms, in which the decrease in the anatoxin-A intensity over time under light illumination can be clearly observed, yielding 93% degradation in 240 min. The TOC measurements showed that the supported MoS_2/Cu_2O catalysts achieved a high mineralization rate of 86% (Fig. 7b). The rate constant of the anatoxin-A photodegradation, following a pseudo-first-order kinetics (Fig. 7c), was 0.011 min^{-1} (k_N = 151 min^{-1} g^{-1}). These results suggest that the solvothermal MoS_2/Cu_2O nanoflakes are extremely efficient for cyanotoxins removal as compared with previous studies[115] and, importantly, without using any noble metal as co-catalyst.[114]

To further evaluate the photocatalytic performance of the MoS_2/Cu_2O composite under more realistic conditions, we investigated its activity in mixed-pollutant systems containing both anatoxin-A (10 ppm) and tetracycline (10 ppm), in Milli-Q

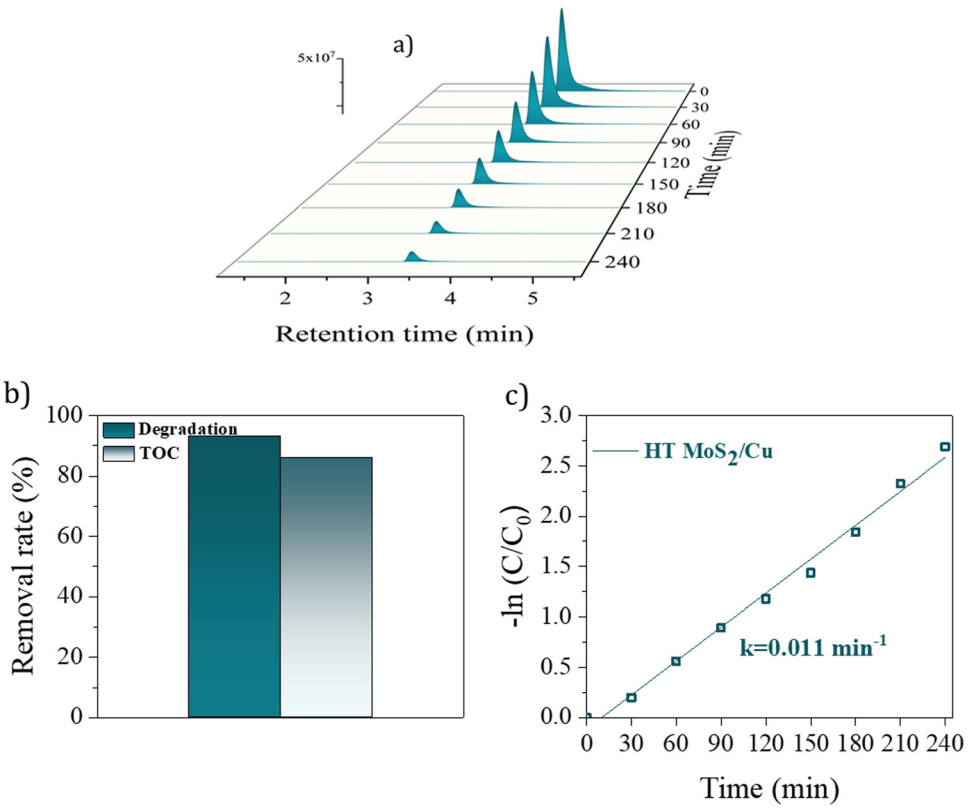

Fig. 7 Analysis of anatoxin-A degradation and kinetics. (a) The decrease in absorbance of anatoxin-A at its retention time passing through a chromatography column. (b) Degradation and TOC rates. (c) Linear fitting of the rate constant (k).

water and tap water, at pH values of 6 and 8. Total organic carbon (TOC) measurements were employed to assess the extent of mineralization achieved during photocatalysis. In Milli-Q water, the mineralization efficiency reached 67.2% at pH 6 and 74.1% at pH 8 after 180 minutes of illumination, increasing to 81.3% and 85.3%, respectively, after 240 minutes. Notably, in tap water, the mineralization rates were even higher, achieving 83.5% at pH 6 and 87.4% at pH 8 after 180 minutes, and further improving to 92.5% and 96.1% at 240 minutes. These results highlight the robust performance of the catalyst and adaptability in more complex aqueous environments, demonstrating its potential applicability in practical water treatment scenarios. Detailed experimental conditions and supporting data are provided in the ESI.†

2.3. Supported MoS_2/Cu_2O nanoflakes as photodynamic agents with NIR light

The observed photocatalytic efficiency of the SiO_2-MoS_2/Cu_2O heterostructures in generating ROS under visible light motivated analyzing their potential as photodynamic agents for biomedical applications. To date, studies investigating MoS_2 as a photodynamic agent for biomedical therapies remain limited. Only a few studies have explored MoS_2 quantum dots or flakes combined with heterostructures for bacterial disinfection or antimicrobial activity,[18,29,117–119] with even fewer focusing on ROS-based approaches for tumoral cells.[120] Instead, most biomedical research has centered on the MoS_2 exceptional photothermal conversion efficiency, highlighting its use as a photothermal agent.[121,122] A recent study has also addressed the use of Cu_2O-loaded MoS_2 nanoflowers, specifically designed for intracellular ROS generation through chemodynamic (Fenton-like) reactions, relying on Cu^+-catalyzed hydrogen peroxide decomposition, and photothermal effects under NIR-II (1064 nm) irradiation at high power densities.[123] Moreover, some efforts have explored combining photothermal and photodynamic therapies involving MoS_2, although these often rely on additional materials acting as photosensitizers.[121,124]

In light of these gaps, we investigated the catalytic efficiency of the supported MoS_2/Cu_2O using NIR light illumination (within the first biological window with higher penetration into the tissues) under physiological conditions (cell medium and 37 °C). To demonstrate the strength and long-distance action of the generated ROS, as proof of concept, the supported MoS_2/Cu_2O nanoflakes were placed over Saos-2 bone cancer cells maintaining a separation distance of 120 μm, as depicted in Fig. S13a (ESI†). Two different NIR illumination wavelengths were used to trigger the nanoflakes ROS production: a 660 nm LED and a 808 nm laser, both with an intensity of 100 mW cm^{-2} (well below the maximum permissible light exposure[125]). The photoinduced effect by the nanoflakes on the Saos-2 cells viability was evaluated using a live/dead test 24 h after the illumination. Live and dead cells were counted in five different sites from three replicas, and were normalized with respect to the control.

Firstly, we analyzed, as control experiments, the effect of the 660 nm illumination for 90 min and the supported photocatalyst without illumination on the cell viability. As Fig. 8a and f show, the 660 nm induced only a slight reduction of the viability, thus corroborating that this wavelength is safe in shorter exposures, as expected from other studies at the same wavelength and with higher intensity.[121] On the other hand, the supported MoS_2/Cu_2O nanostructures exhibited a complete lack of toxicity in the darkness (Fig. 8b and f).

Next, we studied the effects of the supported catalysts exposed to the 660 nm light for increasing times (Fig. 8c–e). As can be observed, after only 15 min of light exposure, there was a significant reduction of cell viability, with large reduction in the number of live cells and a considerable percentage of dead cells, thereby reducing the viability to only 44%. Increasing the illumination time to 30 min further reduced the number of live cells and increased the amount of detected death cells, yielding a viability of just 14%. Finally, after 90 min, less than 5% of the cells remained alive. Therefore, the NIR LED at 660 nm with an intensity of 100 mW cm^{-2} proved high efficiency in the ROS production, inducing a remarkable cell death in a time-dependent manner. To further validate that the photodynamic effects originate exclusively from the MoS_2/Cu_2O heterostructure, we performed additional viability assays using supported pure Cu_2O or pure MoS_2 under the same NIR illumination conditions. The results, presented in Fig. S14 in the ESI,† demonstrate that both individual components exhibit minimal photodynamic activity when used separately. Moreover, the high cell viability observed after 30 minutes of illumination in the presence of the SiO_2/Cu_2O photocatalyst suggests that the potential cytotoxicity typically associated with copper ion leaching is also negligible. All these findings are also consistent with the low degradation efficiency of organic pollutants previously reported for the pure systems, and highlights the critical role of the MoS_2/Cu_2O interface in enabling efficient ROS generation and enhanced photodynamic response.

To assess the biomedical applicability with light showing deeper penetration into the tissues and higher maximum exposure levels, the same assay was carried out using a 808 nm NIR laser at 100 mW cm^{-2} during 30 min. In this case, the control of 808 nm light exposure yielded nearly 100% of alive cells (Fig. 9a and c), which confirms the higher safety of the 808 nm NIR light compared to the 660 nm light. Nevertheless, when the nanoflakes were irradiated with the 808 nm laser for 30 min, only 16% of the cells remained alive (Fig. 9b–d), therefore causing a similar effect as the 660 nm LED. A slight increase in the irradiation time or intensity could achieve a complete elimination of the cancer cells.

As potential photodynamic therapy, it is relevant to investigate the type of cell death caused by the illuminated MoS_2/Cu_2O nanostructures. Apoptosis emerges as the preferred programmed cell death, as it holds the potential for therapeutic benefits while minimizing the adverse effects associated with alternative cell deaths, such as necrosis. The presence of apoptotic cells was detected *via* Annexin V/PI protocol through confocal microscopy. During apoptosis, phosphatidyl serine (PS) translocate from the inner to the outer leaflet of the plasma membrane. Fluorescent Annexin V binds with high affinity to

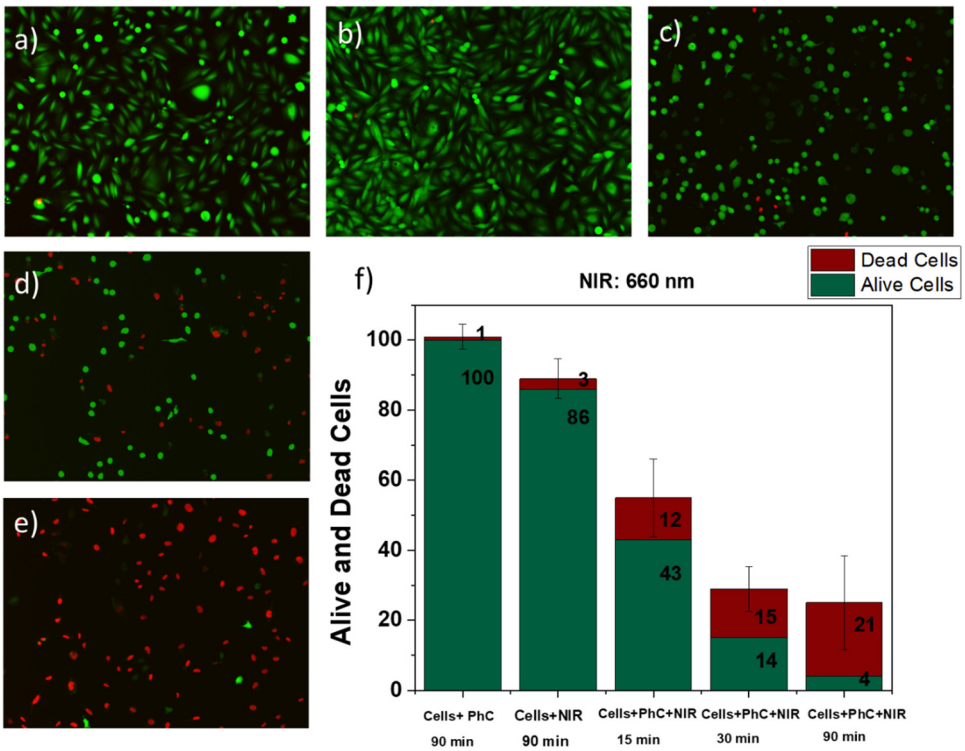

Fig. 8 Viability of Saos-2 cells. Representative live/dead images of: (a) cells exposed to NIR at 660 nm and 100 mW cm^{-2} for 90 min, and (b) cells exposed to immobilized photocatalyst (PhC) for 90 min without light. (c)–(e) Cells incubated with supported photocatalyst and exposed to 100 mW cm^{-2} of 660 nm NIR light for different times: (c) 15 min, (d) 30 min, and (e) 90 min. (f) Percentage of alive (green) and dead (red) cells in the different conditions. Note that the reduction in the total number of live plus death cells as the illumination time increases is due to the already detached death cells, which are washed away during the detection process.

PS, being a marker for the initial stages of apoptosis. *In vitro*, as apoptosis progresses, DNA fragmentation and membrane permeabilization occur, which are characteristic of late-stage apoptosis. In this case, PI enters the cells and binds to the nucleic acid. Therefore, the presence of red fluorescence in the nucleus is an indicator of the late-stage apoptosis. In our study, Saos-2 cells were incubated with the supported MoS_2/Cu_2O nanoflakes and illuminated with 808 nm laser for 30 min. After this time, the few remaining cells exhibited typical features present in apoptotic cells as presence of blebs and condensed nucleus (Fig. S13b, ESI†). These features suggest apoptosis as a possible cell death mechanism. As further confirmation, the annexin V/PI analysis (Fig. 9d) showed that 57% of the cells were positively stained with annexin V, thus undergoing apoptosis. From this set of cells, 34% were negatively stained to PI, reflecting intact membranes where PI was not yet bound to nucleic acids, thus being at an early stage of apoptosis. The remaining 66% of the apoptotic cells stained positively for both annexin V and PI, being consequently in the late apoptosis stage. Therefore, the generated ROS triggered by the supported MoS_2/Cu_2O nanostructures efficiently induced the dead of the Saos-2 cells by apoptosis by using safe low intensity NIR light.

With respect to a plausible mechanism for the apoptosis induction, it is proposed that ROS generated by the MoS_2/Cu_2O system initiate cell death primarily through oxidative damage to the cell membrane, rather than intracellular pathways. Before we have seen that the main photogenerated ROS are superoxide anions and hydroxyl radicals, which are known for their high reactivity and short lifetimes. Considering the experimental configuration, where MoS_2/Cu_2O nanoflakes are immobilized and separated from the cultured cancer cells by a 120 μm gap, it is highly unlikely that these ROS reach the cytoplasm. Instead, the photodynamic effect is presumed to occur extracellularly, at the outer cell membrane. The ROS likely induce oxidative damage by initiating lipid peroxidation and modifying membrane proteins, ultimately disrupting membrane integrity and triggering apoptosis through external signaling pathways.[126] This hypothesis is further supported by the intracellular ROS measurements, which showed no significant increase in ROS levels within the cells after illumination of the MoS_2/Cu_2O nanoflakes for 30 min (see ESI,† Fig. S15).

This approach could offer a promising alternative to the use of the conventional photosensitizers, thereby enhancing photodynamic performance through the efficient generation of cytotoxic ROS on cancer cells. Moreover, by increasing the 808 nm light intensity (*e.g.*, at 300 mW cm^{-2}, which remains well below the maximum permissible exposure level[125]), combined photothermal and photodynamic effects could be achieved using a single light source. This approach could significantly reduce the light exposure time to completely kill cancer cells. It is important to note that, while the present study did not include experiments with normal bone cells due to the considerable

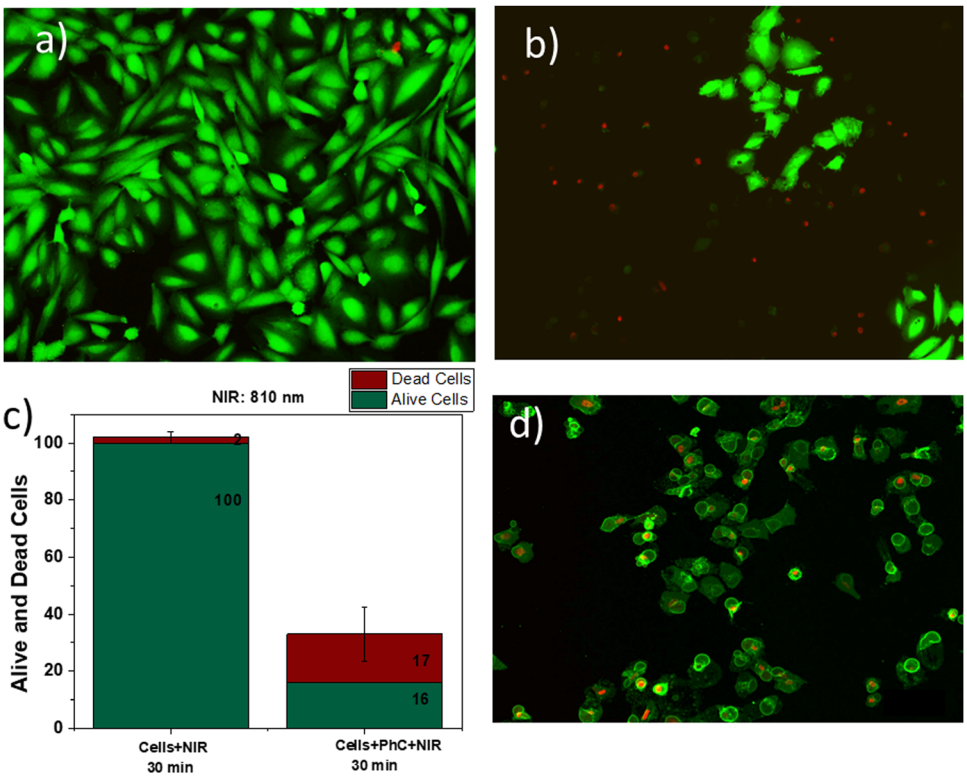

Fig. 9 Viability and apoptosis detection of Saos-2 cells under 808 nm illumination (100 mW cm^{-2} for 30 min). Representative live/dead images of: (a) control cells without MoS_2/Cu_2O exposed to NIR, and (b) cells incubated with supported nanoflakes and exposed to NIR. (c) Percentages of alive (green) and dead (red) cells in both conditions. (d) Fluorescence image showing early and late apoptotic cells, in which annexin V binds to the translocated PS (green) and PI binds to DNA (red).

challenges involved in obtaining, culturing, and maintaining these cells, previous studies by our group using other photosensitive agents and comparing normal and tumoral human cell lines have shown a tendency toward selective cytotoxicity in cancer cells.[127] These earlier findings suggest that our current photocatalytic system could potentially exhibit similar behavior.

2.4. Analysis of the photocatalytic pathway

The characterization techniques have shown that, apart from the already good visible light absorption characteristics of MoS_2, the presence of Cu_2O further promotes the efficiency of light absorption. The Cu_2O heterojunction also contributes to improve the charge separation of the photocarriers. The lack of photoluminescence of the overall MoS_2/Cu_2O nanoflakes also indicates its excellent photocatalytic activity due to a lower electron-pair recombination rate. Moreover, the presence of the additional T′ phase in the solvothermal MoS_2 provides more conductivity and high density of exposed active basal, edge and defect sites as compared to a pure 2H-MoS_2 phase. These sites serve as catalytic sites for the redox processes of the analytes at the liquid interface. Moreover, the growth of MoS_2 on a high mesoporous silica support introduces more defects and opens stacking layers, driven by support-induced strain and ion intercalation, significantly expanding the interlayer spacing, weakening van der Waals interactions, and enhancing electrolyte penetrability and access to catalytic sites. Collectively, these factors synergistically enhance the photocatalytic performance of the hybrid system.

To better understand the photocatalytic degradation pathway, we have measured the bandgap of the Cu_2O and the solvothermally synthesized MoS_2, along with their corresponding valence and conduction band edges. Band-gap measurements were performed using Kubelka–Munk analysis (details in the ESI,† Fig. S10a and b). The measured band gaps were 1.97 eV for MoS_2 and 1.89 eV for Cu_2O. The E_{gap} value of MoS_2 is slightly higher than expected for 2H-phase MoS_2, which could be attributed to some contributions of molybdenum oxide, as suggested by the XPS analysis.

A proposed photocatalytic degradation mechanism has been hypothesized based on photoemission measurements (Fig. 10), which provided a more accurate determination of the valence band maximum relative to the vacuum level (see ESI† for details).

Precisely defining electron transfer pathways in this system remains challenging due to the inherent complexity of the materials involved due to the polyphasic nature of MoS_2, containing both 2H and 1T′ phases, along with some contribution of molybdenum oxide. Furthermore, interfacing Cu_2O with this multiphase MoS_2 introduces an additional level of complexity. The spatial arrangement of these nanostructures, specifically, whether the 2H or 1T′ phases are more in direct contact with Cu_2O, can significantly influence charge transfer pathways and the overall reaction mechanism. This structural variability

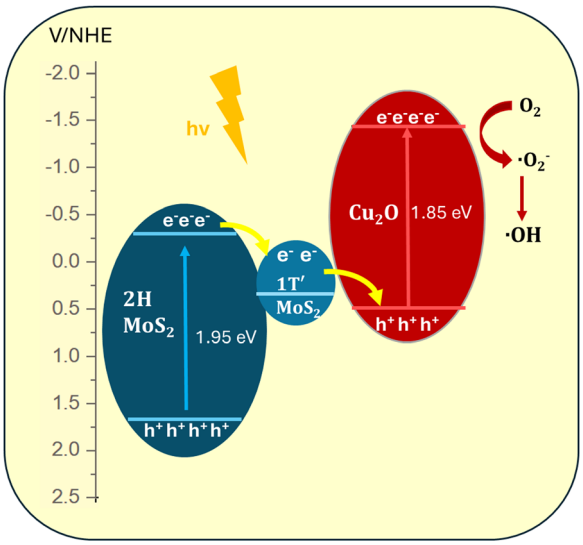

Fig. 10 Schematic of photocatalytic degradation mechanism of solvothermal MoS_2/Cu_2O.

introduces uncertainties that cannot be fully captured by simple band alignment models.

Nonetheless, based on our characterization, it can be reasonably assumed that the 1T′ phase is dominant within the MoS_2 structure, and that Cu_2O nanostructures are more likely interfacing with the 1T′ phase, while also the 1T′ phase maintaining contact with the semiconducting 2H phase. With this assumption, a band diagram has been constructed accordingly. Photoemission measurements revealed that the VBM of the 2H-MoS_2 phase lies at a more positive potential than that of Cu_2O, whereas the VBM of the 1T′ phase is positioned at a less positive potential than that of Cu_2O (see Fig. S11c, ESI†). By combining these VBM values with band gap estimations from absorption spectroscopy, we inferred the conduction band positions for each component and constructed the hypothetical band diagram of Fig. 10. The resulting diagram, referenced to the normal hydrogen electrode (NHE) scale, suggests that the system could operate *via* a Z-scheme mechanism, enhancing charge separation and photocatalytic efficiency. Under light illumination, electrons from the valence band (VB) of 2H-MoS_2 are excited to its conduction band (CB) and can subsequently transfer to the CB of 1T′-MoS_2, which could mainly act as an electron mediator due to its more metallic character. These electrons could then recombine with holes in the VB of Cu_2O, facilitating charge recombination at this interface. Meanwhile, photoexcited electrons in the CB of Cu_2O remain available to reduce molecular oxygen, generating superoxide radicals ($^{\bullet}O_2^-$), which subsequently react with water to form hydroxyl radicals ($^{\bullet}OH$). These have been the main ROS components detected by chemical quenching with selective ROS scavengers and EPR. The holes remaining in the VB of 2H-MoS_2 could contribute to alternative oxidation pathways during analyte degradation. However, the generation of hydroxyl radicals *via* direct oxidation of water by these holes is unlikely, as it requires redox potentials of approximately 2.8 eV (depending on pH), and in this case the VB levels of MoS_2 remain below 2 eV. Moreover, this charge pathway could explain the remarkably stability of Cu_2O during the degradation process. This stability could be likely facilitated by the 1T′-MoS_2 phase, which may act as an electron mediator, supplying electrons to the valence band of Cu_2O, thereby stabilizing its oxidation state. This electron transfer pathway contributes to maintaining a sustainable source of photocarriers and supports the long-term operational stability of the photocatalyst system. Eqn (1)–(4), illustrate the possible reaction pathway.

$$Cu_2O/T' - 2H\ MoS_2 + h\upsilon \rightarrow ((Cu_2O/T' - 2H\ MoS_2))^* + e^- + h^+ \quad (1)$$

$$O_2 + e^- \rightarrow {}^{\bullet}O_2^- \quad (2)$$

$${}^{\bullet}O_2^- + H_2O \rightarrow H_2O_2 + {}^{\bullet}OH \quad (3)$$

$$\text{Analyte} + h^+/{}^{\bullet}O_2^-/{}^{\bullet}OH \rightarrow \text{Degraded products} \quad (4)$$

3. Conclusions

2D MoS_2 nanoflakes were successfully grown on supported mesoporous silica nanoparticles by solvothermal treatment using a single precursor serving as both the Mo and S source. The characterization suggests that the most likely structure of the solvothermal MoS_2 is a combined 2H-1T′ phase, featuring higher density of catalytic sites (basal, edge defect active sites) and expanded stacking layers, which promote electrolyte penetrability and the transfer of photogenerated charges to analytes at the liquid interface. The deposition of an extremely thin layer of Cu greatly enhances the photocatalytic properties of the system. Cu in the form of the semiconducting Cu_2O promotes light absorption and charge separation. The synergistic effect of all these features makes the photocatalytic performance of MoS_2/Cu_2O nanoflakes superior to that of the bare MoS_2 towards tetracycline and anatoxin-A degradation and mineralization with white light. Moreover, the MoS_2/Cu_2O nanoflakes were stable even after 10 cycles. It is important to highlight the use of an ultralow amount of photocatalyst to achieve effective contaminant degradation and a high degree of mineralization, surpassing reported studies. This outstanding performance, combined with the low amount of material usage and excellent recyclability, highlights the system's sustainability. In addition, the catalytic activity of the MoS_2/Cu_2O nanoflakes was tested on cancer cells *in vitro* under NIR light irradiation. They showed negligible cytotoxicity in darkness and efficient cancer cells elimination under NIR light irradiation. Overall, we anticipate that the environmentally friendly, cost-efficient solvothermal supported MoS_2/Cu_2O nanoflakes could be a potential catalyst not only for environmental applications but also for biomedical applications, especially for NIR photodynamic cancer treatment.

4. Materials and methods

4.1. Synthesis and self-assembly of mesoporous silica nanoparticles

A surfactant-template method based on the Stöber approach was chosen to synthesize mesoporous silica nanoparticles.[36] First, 1.02 g of cetyltrimethylammonium bromide (CTAB) surfactant was dissolved in 340 mL distilled water in a 500 mL Erlenmeyer flask and sonicated until clear. The solution was heated to 30–35 °C in an oil bath, followed by the addition of 120 mL absolute ethanol and 1.5 mL of 35% NH_3 under vigorous stirring, facilitating the formation of uniform spherical micelles. Tetraethyl orthosilicate (TEOS) was added dropwise (1.5 mL) at 80 °C. Additionally, 1 mL of trimethylbenzene (TMB) was introduced as a pore-expanding agent. The reaction was maintained at 80 °C for 2 hours. Then the suspension was centrifuged and washed in ethanol three times. To remove the CTAB template, a solvent extraction strategy was used. The nanoparticle dispersion was subjected to an ethanolic solution of ammonium nitrate (0.0038 M), heated at 80 °C, and maintained under constant stirring for 1 hour. The dispersion was then washed three times with ethanol *via* centrifugation steps. Nanoparticles with sizes around 230 nm and pore sizes of approximately 35 nm were obtained.

For the self-assembly process, a capillarity-mediated self-assembly at a liquid/air interface was performed. To achieve this, a silicon wafer was placed on a slanted support inside a tank. The tank was filled with distilled water until the wafer was submerged. The colloidal dispersion of silica (4 mL) contained in a syringe and connected to a high-precision peristaltic pump was injected directly at the air–liquid interface up to form a floating monolayer of nanoparticles. The tank was then slowly drained at a rate not exceeding 5.5 mL s^{-1} until the nanoparticles were completely transferred to the silicon support. The assembled nanoparticles were further subjected to oxygen plasma cleaning (400 W, 60 sccm O_2, 4 min).

4.2. Synthesis of MoS_2/Cu_2O nanoflakes on mesoporous SiO_2 nanoparticles

As the mesoporous silica nanoparticles are negatively charged, a silanization process was needed to grow the MoS_2 flakes on the silica surface. For this purpose, the substrate was immersed in (3-aminopropyl)triethoxysilane (APTES) 4% solution in toluene for 2 h at 80 °C. Then, the substrate was rinsed with toluene and immersed in DI water for 2 h to clean the excess of APTES. For the solvothermal growth of MoS_2, 0.3 mg of ammonium tetrathiomolybdate ($(NH_4)_2MoS_4$) was dissolved in 10 mL dimethylformamide (DMF) and the solution was sonicated for 30 min. Subsequently, the substrate was submerged in DMF solution, transferred to a stainless-steel autoclave, and solvothermally treated for 18 h at 180 °C. After 18 h, the as-prepared sample was rinsed with water and dried with a nitrogen gun. Finally, 3 nm copper (Cu) was deposited onto the MoS_2 nanoflakes *via* e-beam deposition and exposed to air. The mass and molar ratios of Cu_2O to MoS_2 in the Silica/MoS_2/Cu_2O system were determined based on elemental analysis using inductively coupled plasma mass spectrometry (ICP-MS). This method enabled precise quantification of the copper and molybdenum content within the composite. Based on these measurements, the mass ratio of MoS_2 to Cu_2O was 6.2, while the molar ratio was 5.6. For the MoS_2 samples grown by chemical vapor deposition (CVD), an alumina boat with a precursor MoO_3 (5 mg) was placed in the middle of the quartz tube furnace. Then the wafer (4 cm^2) with the mesoporous silica nanoparticles was placed onto the alumina boat in an upside-down manner. Another alumina boat was inserted at the cold side of the quartz tube at a distance of 15 cm with sulfur powder as the other reagent precursor. The furnace was heated up to 750 °C at a rate of 50 °C min^{-1} under Ar (at a flow of 40 sccm) to induce the reaction. After 25 min growth time, the furnace was rapidly cooled down.

4.3. Structural, morphological, and spectroscopic characterization of the photocatalyst

Scanning electron microscopy (SEM) measurements were conducted using a FEI Magellan 400L XHR SEM microscope, while transmission electron microscopy (TEM) images were captured with a Thermo Fisher Scientific Spectra 300 (S)TEM. X-ray diffraction (XRD) analysis was carried out using a Malvern PANalytical X'pert Pro MPD, and Raman/photoluminescence analysis were performed with a Horiba T64000 spectrometer. X-ray photoelectron spectroscopy (XPS) experiments were carried out using a SPECS PHOIBOS150 hemispherical analyzer with a monochromatic X-ray source (1486.6 eV) operated at 300 W. The reported binding energies were obtained with an error of ±0.1 eV and were referred to the Fermi level of the analyzer, which is periodically determined by measuring the photoelectron energies from an atomically clean reference Au(111) sample. No corrections to the binding energies have been applied. The estimated overall energy resolution (analyzer and photons) is better than 0.6 eV at a pass energy of 20 eV.[50] Least-squares fits of the experimental data after a Shirley-type background subtraction has been obtained using a combination of Gaussians and Lorentzian functions. The branching ratios for the Mo3d and S2p doublets were set to 2/3 and 1/2, respectively, and the spin–orbit splitting was fixed to 3.16 and 1.19 eV, respectively. For all samples, the binding energy of C1s is 284.5 ± 0.1 eV, arising from graphitic carbon contamination, so that charging effects can be ruled out. The valence band maximum (VBM) was obtained by a linear extrapolation of the leading edges in the valence band spectra using both XPS and ultraviolet photoelectron spectroscopy (UPS) and the ionization potentials (IP), by subtracting the spectral width, *i.e.*, the difference between the onset of photoemission (secondary electrons cut-off, SECO) and the VBM, while applying a −10 V bias to the sample to clear the analyzer work function, to the 21.22 eV energy used in UPS.[128]

Electron paramagnetic resonance (EPR) measurements were performed using a Bruker Elexsys 580 spectrometer operating in X-band (9.858 GHz), with a Bruker ER4122SHQE superhigh-Q cylindrical resonator. Spectra were recorded in continuous-wave (CW) mode at room temperature using a microwave power

of 4.7 mW and a modulation amplitude of 0.3 mT to avoid signal saturation and distortion. For radical spin trapping, 50 μL of DMPO solution (90 mM or 0.5 M, depending on the sample) in deionized water was applied directly to the device surface. After optional irradiation with visible light, the solution was transferred to Hirschmann capillary tubes and sealed with Critoseal®. Spectral simulations were performed using the EasySpin software package.[129]

4.4. Photodegradation characterization

The MoS_2/Cu_2O photocatalyst (4 cm^2) was immersed in a solution containing 5 ppm tetracycline (TC) (pH = 6 and pH = 8) or 20 ppm anatoxin-A. The system was kept in the dark for 30 min to reach adsorption equilibrium. Afterward, the nanoreactors were irradiated with visible light using a warm LED ($\lambda > 420$ nm, max. 600 nm, 52×10^{-3} W cm^{-2}). During all photodegradation experiments, the reaction solution was continuously agitated using a magnetic stirrer to ensure homogeneous mixing and effective contact between the immobilized photocatalyst film and the pollutants. In the case of TC, the photoreaction progress was monitored *via* absorbance measurements in the case of TC using a Cary 4000 spectrophotometer. For anatoxin-A, the composition was analyzed *via* high-performance liquid chromatography (HPLC) using a Waters Alliance 2795 instrument equipped with a PDA detector (Waters 2996) and a mass detector (Waters ZQ 2000). The mineralization efficiency was evaluated using a TOC-VCSH equipment (Shimadzu) with a high-sensitivity column.

4.5. Cell viability analysis

Supported MoS_2/Cu_2O nanoflakes (size 1 cm^2) were UV-sterilized to avoid any contamination before placing them inside the cell media. To check the biocompatibility of the cells with the nanophotocatalysts and NIR light separately, a live/dead viability/cytotoxicity assay was performed. In a 35 mm Petri dish, a thin double-sided adhesive spacer was placed. Saos-2 cells were seeded only inside the spacer at a density of 10 000 cells. After 48 h, different conditions were tested: (i) cells exposed to 660 nm LED for 90 min, (ii) cells exposed to 808 nm laser for 30 min, (iii) cells incubated with immobilized photocatalysts for 90 min, (iv) cells incubated with immobilized photocatalysts and exposed to 660 nm LED for 15, 30 or 90 min, (v) cells incubated with immobilized nanophotocatalysts and exposed to 808 nm laser for 30 min. In the next step, the wafers were removed, and the cells were kept at standard conditions (37 °C, 5% CO_2) for 24 h. Then the cells were analyzed with the live/dead kit according to manufacturer's instructions. Images from different sites were taken by Olympus inverted microscope equipped with epifluorescence. Note that the wafer size is 1 cm^2 with an amount of 18.25 μg cm^{-2} of photocatalyst.

4.6. Apoptosis detection

Annexin V/propidium iodide (PI) assay was employed to determine the nature of cell death, specifically focusing on apoptosis. In a 35 mm Petri dish, a thin double-sided adhesive spacer was placed. Saos-2 cells were seeded only inside the spacer at a density of 10 000 cells. After 48 h, cells were incubated with UV-sterilized immobilized nanophotocatalysts (wafer size: 1 cm^2, 18.25 μg cm^{-2} nanoreactors amount) and exposed to 808 nm laser for 30 min. Then, the wafer was removed, and cells were kept in standard conditions (37 °C, 5% CO_2) for 4 h. In the last step, cells were stained with a mix of annexin V and PI according to manufacturer's instructions. Images from different sites were taken by Olympus inverted microscope equipped with epifluorescence.

Author contributions

G. S. conducted part of the experiments on photocatalyst characterization, pollutant degradation, and data curation. J. C. R. conducted photocatalyst characterization and data curation. N. A. B., A. L. and C. V. conducted the biological experiments and data curation, M. S. performed Raman characterization and V. N. conducted EPR measurements, J. F. contributed to photocatalyst characterization through XPS/UPS measurements. C. N. supervised the biological experiments and characterization. J. N. supervised the research and contributed to the writing of the paper. A. S. supervised and conducted part of the experiments on pollutant degradation. B. S. conceived the idea, supervised the research, and contributed to the writing of the paper. M. J. E. conceived the idea, supervised the research, and contributed to the writing of the paper.

Data availability

The authors declare that the data supporting the findings of this study are available at CSIC Digital repository at **https://doi.org/10.20350/digitalCSIC/17050**.

Conflicts of interest

The authors declare that they have no known competing financial interests or personal relationships that could have appeared to influence the work reported in this paper.

Acknowledgements

The Ministerio de Ciencia e Innovación (MICIN) is acknowledged through Grants DIN2021-011916, TED2021-129898B-C22, TED 2021-129898B-C21, TED2021-132040B-C22, PID 2020-116844RB-C21, PID2022-138588OB-C31, PID2022-138588OB-C32 and PID 2021-124568NB-I00 funded by NextGenerationEU and MICIU/AEI/10.13039/501100011033. The authors also would like to express their gratitude to the Departament de Recerca i Universitats, particularly the Departament d'Acció Climàtica, Alimentació i Agenda Rural, as well as the Fons Climàtic de la Generalitat de Catalunya (project 2023 CLIMA 00009 AGAUR) for their support. We also acknowledge funding from Generalitat de Catalunya through the 2021-SGR-00651 project. ICN2 is funded by the CERCA program/Generalitat de Catalunya. The ICN2 is supported by the Severo Ochoa Centres of Excellence program, Grant

CEX2021-001214-S, and the IMB is supported by the Maria de Maeztu Centres of Excellence program Grant CEX2023-001397-M, both funded by MCIU/AEI/10.13039/501100011033. Authors thank the Service of Chemical Analysis and Microscopy at the Universitat Autònoma de Barcelona, the CCiT-UB for the use of their equipment and Josep Martí for his assistance with HPLC analysis and also thank G. Sauthier (ICN2) for the support with XPS measurements. Authors also acknowledge the use of instrumentation as well as the technical advice provided by the Joint Electron Microscopy Center at ALBA (JEMCA) and funding from Grant IU16-014206 (METCAM-FIB) to ICN2 funded by the European Union through the European Regional Development Fund (ERDF), with the support of the Ministry of Research and Universities, Generalitat de Catalunya.

References

1 H. Wang, C. Li, P. Fang, Z. Zhang and J. Z. Zhang, *Chem. Soc. Rev.*, 2018, **47**, 6101–6127.
2 D. Voiry, A. Mohite and M. Chhowalla, *Chem. Soc. Rev.*, 2015, **44**, 2702–2712.
3 H. L. Zhuang, M. D. Johannes, A. K. Singh and R. G. Hennig, *Phys. Rev. B*, 2017, **96**, 165305.
4 D. Pariari and D. D. Sarma, *APL Mater.*, 2020, **8**, 040909.
5 Z. Li, X. Meng and Z. Zhang, *J. Photochem. Photobiol., C*, 2018, **35**, 39–55.
6 Z. Lei, J. Zhan, L. Tang, Y. Zhang and Y. Wang, *Adv. Energy Mater.*, 2018, **8**, 1703482.
7 V. Yadav, S. Roy, P. Singh, Z. Khan and A. Jaiswal, *Small*, 2019, **15**, 1803706.
8 Z. Wang and B. Mi, *Environ. Sci. Technol.*, 2017, **51**, 8229–8244.
9 S. Shi, Z. Sun and Y. H. Hu, *J. Mater. Chem. A*, 2018, **6**, 23932–23977.
10 J. Strachan, A. F. Masters and T. Maschmeyer, *J. Mater. Chem. A*, 2021, **9**, 9451–9461.
11 Z. Xia, Y. Tao, Z. Pan and X. Shen, *Results Phys.*, 2019, **12**, 2218–2224.
12 A. Ambrosi, Z. Sofer and M. Pumera, *Chem. Commun.*, 2015, **51**, 8450–8453.
13 R. Peng, L. Liang, Z. D. Hood, A. Boulesbaa, A. Puretzky, A. V. Ievlev, J. Come, O. S. Ovchinnikova, H. Wang, C. Ma, M. Chi, B. G. Sumpter and Z. Wu, *ACS Catal.*, 2016, **6**, 6723–6729.
14 W. Q. Chen, L. Y. Li, L. Li, W. H. Qiu, L. Tang, L. Xu, K. J. Xu and M. H. Wu, *Engineering*, 2019, **5**, 755–767.
15 Y. F. Zhao, Z. Y. Yang, Y. X. Zhang, L. Jing, X. Guo, Z. Ke, P. Hu, G. Wang, Y. M. Yan and K. N. Sun, *J. Phys. Chem. C*, 2014, **118**, 14238–14245.
16 D. Wang, X. Zhang, S. Bao, Z. Zhang, H. Fei and Z. Wu, *J. Mater. Chem. A*, 2017, **5**, 2681–2688.
17 Y. Yu, L. Lu, Q. Yang, A. Zupanic, Q. Xu and L. Jiang, *ACS Appl. Nano Mater.*, 2021, **4**, 7523–7537.
18 L. Chen, C. P. Huang, Y. Chuang, T. B. Nguyen, C. W. Chen and C. Di Dong, *New J. Chem.*, 2022, **46**, 14159–14169.
19 M. Chen, W. Chang, J. Zhang, W. Zhao and Z. Chen, *ACS Omega*, 2023, **8**, 15458–15466.
20 X. Hua, H. Chen, Z. Wang, C. Rong, D. Dong, J. Qu, N. Zheng, Z. Guo, D. Liang and H. Liu, *Sep. Purif. Technol.*, 2024, **347**, 127632.
21 Y. R. Liu, J. H. Wu, X. Z. Wang, C. Y. Li, Y. X. Cai, H. H. Xing, S. S. Xia, J. Q. Zhao, W. Zhao and Z. Chen, *Fuel Cells*, 2024, e202400040.
22 L. Tian, R. Wu and H. Y. Liu, *J. Mater. Sci.*, 2019, **54**, 9656–9665.
23 C. Liu, D. Kong, P. C. Hsu, H. Yuan, H. W. Lee, Y. Liu, H. Wang, S. Wang, K. Yan, D. Lin, P. A. Maraccini, K. M. Parker, A. B. Boehm and Y. Cui, *Nat. Nanotechnol.*, 2016, **11**, 1098–1104.
24 X. Hu, X. Zeng, Y. Liu, J. Lu, S. Yuan, Y. Yin, J. Hu, D. T. McCarthy and X. Zhang, *Appl. Catal., B*, 2020, **268**, 118466.
25 Y. Li, H. Li, X. Lu, X. Yu, M. Kong, X. Duan, G. Qin, Y. Zhao, Z. Wang and D. D. Dionysiou, *J. Colloid Interface Sci.*, 2021, **596**, 384–395.
26 X. Bai, X. Wang, T. Jia, L. Guo, D. Hao, Z. Zhang, L. Wu, X. Zhang, H. Yang, Y. Gong, J. Li and H. Li, *Appl. Catal., B*, 2022, **310**, 121302.
27 M. Rezaei, A. Nezamzadeh-Ejhieh and A. R. Massah, *Energy Fuels*, 2024, **38**, 7637–7664.
28 X. Hua, H. Chen, C. Rong, F. Addison, D. Dong, J. Qu, D. Liang, Z. Guo, N. Zheng and H. Liu, *J. Hazard. Mater.*, 2023, **448**, 130951.
29 H. Li, Q. Xia, X. Liu, L. Hu, J. Zhong, F. Lu, Y. Chen, Z. Hu and W. Gao, *J. Environ. Chem. Eng.*, 2024, **12**, 112447.
30 H. Huang, Y. Lei, L. Bai, Y. Liang and H. Yang, *Colloids Surf., A*, 2023, **657**, 130558.
31 H. Zhang, M. Huo, R. Jia, S. Xie, Y. Zhong and H. Sun, *ChemistrySelect*, 2023, **8**, e202303766.
32 X. Wu, X. Wang, I. Lynch, Z. Guo, P. Zhang, L. Wu, Y. Deng, Y. Xie, P. Ning and N. Ren, *J. Cleaner Prod.*, 2023, **388**, 135865.
33 L. Luo, X. Shen, L. Song, Y. Zhang, B. Zhu, J. Liu, Q. Chen, Z. Chen and L. Zhang, *J. Alloys Compd.*, 2019, **779**, 599–608.
34 Z. Shi, Y. Zhang, G. Duoerkun, W. Cao, T. Liu, L. Zhang, J. Liu, M. Li and Z. Chen, *Environ. Sci.: Nano*, 2020, **7**, 2708–2722.
35 J. Yu, S. Cong, B. Liu and W. Teng, *J. Environ. Chem. Eng.*, 2022, **10**, 108437.
36 G. Shahnazarova, N. Al Hoda Al Bast, J. C. Ramirez, J. Nogues, J. Esteve, J. Fraxedas, A. Serra, M. J. Esplandiu and B. Sepulveda, *Mater. Horizons*, 2024, **11**, 2206–2216.
37 J. Kang, C. Jin, Z. Li, M. Wang, Z. Chen and Y. Wang, *J. Alloys Compd.*, 2020, **825**, 153975.
38 S. Kumar, V. Sharma, K. Bhattacharyya and V. Krishnan, *Mater. Chem. Front.*, 2017, **1**, 1093–1106.
39 R. Koutavarapu, W. Y. Jang, M. C. Rao, M. Arumugam and J. Shim, *Chemosphere*, 2022, **305**, 135465.
40 M. T. L. Lai, K. M. Lee, T. C. K. Yang, G. T. Pan, C. W. Lai, C. Y. Chen, M. R. Johan and J. C. Juan, *Nanoscale Adv.*, 2021, **3**, 1106–1120.
41 M. T. L. Lai, K. M. Lee, T. C. K. Yang, C. W. Lai, C. Y. Chen, M. R. Johan and J. C. Juan, *J. Alloys Compd.*, 2023, **953**, 169834.

42 A. Castellanos-Gomez, J. Quereda, H. P. van der Meulen, N. Agraït and G. Rubio-Bollinger, *Nanotechnology*, 2016, **27**, 115705.
43 H. Zhao, R. Greco, H. Komsa, R. Sliz, O. Pitkänen, K. Kordas and S. Ojala, *Appl. Catal., B*, 2024, **357**, 124318.
44 Z. Kou, A. Hashemi, M. J. Puska, A. V. Krasheninnikov and H. P. Komsa, *npj Comput. Mater.*, 2020, **6**, 1–7.
45 F. Aryeetey, T. Ignatova and S. Aravamudhan, *RSC Adv.*, 2020, **10**, 22996–23001.
46 S. Mignuzzi, A. J. Pollard, N. Bonini, B. Brennan, I. S. Gilmore, M. A. Pimenta, D. Richards and D. Roy, *Phys. Rev. B:Condens. Matter Mater. Phys.*, 2015, **91**, 195411.
47 J. Aliaga, P. Vera, J. Araya, L. Ballesteros, J. Urzúa, M. Farías, F. Paraguay-Delgado, G. Alonso-Núñez, G. González and E. Benavente, *Molecules*, 2019, **24**, 4631.
48 R. Yang, G. Zhou, C. Wang, Y. Liu, Y. Zhao, Y. Li, X. Fu, J. Chi, X. Chen, H. Fang and Z. Qin, *J. Cleaner Prod.*, 2023, **383**, 135406.
49 F. Nur Indah Sari, M. T. Syue, Y. Purba and J. M. Ting, *Sep. Purif. Technol.*, 2022, **278**, 119650.
50 J. Fraxedas, M. Schütte, G. Sauthier, M. Tallarida, S. Ferrer, V. Carlino and E. Pellegrin, *Appl. Surf. Sci.*, 2021, **542**, 148684.
51 R. Addou, S. McDonnell, D. Barrera, Z. Guo, A. Azcatl, J. Wang, H. Zhu, C. L. Hinkle, M. Quevedo-Lopez, H. N. Alshareef, L. Colombo, J. W. P. Hsu and R. M. Wallace, *ACS Nano*, 2015, **9**, 9124–9133.
52 S. Y. Lee, U. J. Kim, J. Chung, H. Nam, H. Y. Jeong, G. H. Han, H. Kim, H. M. Oh, H. Lee, H. Kim, Y. G. Roh, J. Kim, S. W. Hwang, Y. Park and Y. H. Lee, *ACS Nano*, 2016, **10**, 6100–6107.
53 A. Syari'ati, S. Kumar, A. Zahid, A. Ali El Yumin, J. Ye and P. Rudolf, *Chem. Commun.*, 2019, **55**, 10384–10387.
54 D. Ganta, S. Sinha and R. T. Haasch, *Surf. Sci. Spectra*, 2014, **21**, 19–27.
55 G. T. Kim, T. K. Park, H. Chung, Y. T. Kim, M. H. Kwon and J. G. Choi, *Appl. Surf. Sci.*, 1999, **152**, 35–43.
56 L. Sygellou, *Appl. Surf. Sci.*, 2019, **476**, 1079–1085.
57 H. W. Wang, P. Skeldon and G. E. Thompson, *Surf. Coat. Technol.*, 1997, **91**, 200–207.
58 I. Justicia, P. Ordejón, G. Canto, J. L. Mozos, J. Fraxedas, G. A. Battiston, R. Gerbasi and A. Figueras, *Adv. Mater.*, 2002, **14**, 1399–1402.
59 U. Diebold, *Surf. Sci. Rep.*, 2003, **48**, 53–229.
60 Z. Zhang and J. T. Yates, *Chem. Rev.*, 2012, **112**, 5520–5551.
61 S. McDonnell, R. Addou, C. Buie, R. M. Wallace and C. L. Hinkle, *ACS Nano*, 2014, **8**, 2880–2888.
62 M. C. Biesinger, *Surf. Interface Anal.*, 2017, **49**, 1325–1334.
63 X. Lu, Y. Jin, X. Zhang, G. Xu, D. Wang, J. Lv, Z. Zheng and Y. Wu, *Dalton Trans.*, 2016, **45**, 15406–15414.
64 F. Guo, M. Li, H. Ren, X. Huang, W. Hou, C. Wang, W. Shi and C. Lu, *Appl. Surf. Sci.*, 2019, **491**, 88–94.
65 B. Shaik, R. Atla and T. H. Oh, *J. Mater. Sci.: Mater. Electron.*, 2023, **34**, 853.
66 C. Das, T. Shafi, S. Pan, M. Naushad, B. K. Dubey and S. Chowdhury, *ACS Appl. Nano Mater.*, 2023, **6**, 12991–13000.
67 Z. Mou, J. Xu, T. Meng, X. Wang, R. Gao, J. Guo, S. Gu, Z. Zhou, W. Meng and K. Zhang, *J. Alloys Compd.*, 2023, **967**, 171699.
68 C. Cheng, Q. Shi, W. Zhu, Y. Zhang, W. Su, Z. Lu, J. Yan, K. Chen, Q. Wang and J. Li, *Nanomaterials*, 2023, **13**, 1522.
69 O. C. Olatunde, T. L. Yusuf, N. Mabuba, D. C. Onwudiwe and S. Makgato, *J. Water Process Eng.*, 2024, **59**, 105074.
70 X. Liu, Z. Xing, N. Zhang, T. Cheng, B. Ren, W. Chen, Z. Wang, Z. Li and W. Zhou, *Environ. Sci.: Nano*, 2024, **11**, 3390–3399.
71 C. Das, T. Shafi, L. P. Thulluru, M. Naushad, B. K. Dubey and S. Chowdhury, *ACS ES&T Water*, 2024, **4**, 2144–2158.
72 L. Chen, B. S. Navya and C. Di Dong, *J. Phys. Chem. Solids*, 2024, **193**, 112170.
73 Y. Zeng, N. Guo, H. Li, Q. Wang, X. Xu, Y. Yu, X. Han and H. Yu, *Sci. Total Environ.*, 2019, **659**, 20–32.
74 L. Chen, V. K. Ponnusamy, S. L. Hsieh, S. Hsieh, C. W. Chen and C. Di Dong, *J. Alloys Compd.*, 2022, **892**, 162015.
75 J. Liu, Y. Dong, L. Zhang, W. Liu, C. Zhang, Y. Shi and H. Lin, *J. Cleaner Prod.*, 2021, **322**, 129059.
76 R. Atla and T. H. Oh, *J. Environ. Chem. Eng.*, 2021, **9**, 106427.
77 H. Yi, C. Lai, E. Almatrafi, X. Huo, L. Qin, Y. Fu, C. Zhou, Z. Zeng and G. Zeng, *Chemosphere*, 2022, **288**, 132494.
78 R. Atla and T. H. Oh, *Chemosphere*, 2022, **303**, 134922.
79 Y. Wang, Z. Xing, H. Zhao, S. Song, M. Liu, Z. Li and W. Zhou, *Chem. Eng. J.*, 2022, **431**, 133355.
80 Y. M. Hunge, A. A. Yadav, S. W. Kang and H. Kim, *J. Colloid Interface Sci.*, 2022, **606**, 454–463.
81 R. Ji, C. Ma, W. Ma, Y. Liu, Z. Zhu and Y. Yan, *New J. Chem.*, 2019, **43**, 11876–11886.
82 Y. W. Cui, H. H. Zhang and S. Y. Yu, *RSC Adv.*, 2019, **9**, 35189–35196.
83 F. Guo, X. Huang, Z. Chen, H. Ren, M. Li and L. Chen, *J. Hazard. Mater.*, 2020, **390**, 122158.
84 K. Zhang, W. Meng, S. Wang, H. Mi, L. Sun and K. Tao, *New J. Chem.*, 2019, **44**, 472–477.
85 X. Sheng, H. Qian, J. Lu, H. Lu, K. Hu, Z. Xu, T. Yu and J. Xie, *Mater. Lett.*, 2021, **303**, 130565.
86 Y. Li, Z. Lai, Z. Huang, H. Wang, C. Zhao, G. Ruan and F. Du, *Appl. Surf. Sci.*, 2021, **550**, 149342.
87 W. Li, G. Zhou, X. Zhu, M. Song, P. Wang, C. Ma, X. Liu, S. Han, Y. Huang and Z. Lu, *Appl. Surf. Sci.*, 2021, **555**, 149730.
88 S. Guo, H. Luo, Y. Li, J. Chen, B. Mou, X. Shi and G. Sun, *J. Alloys Compd.*, 2021, **852**, 157026.
89 P. Guo, F. Zhao and X. Hu, *J. Alloys Compd.*, 2021, **867**, 159044.
90 S. Zuo, X. Cao, P. Wang, X. Li, W. Liu, R. Xu, C. Yao, Y. Fu and X. Liu, *Mater. Sci. Semicond. Process.*, 2021, **121**, 105457.
91 E. Vijayakumar, M. Govinda Raj, B. Neppolian, S. Kumar Lakhera and A. John Bosco, *Mater. Lett.*, 2021, **296**, 129891.
92 X. Liu, J. Wang, G. Zhou, L. Tang, Y. Xu, C. Ma, Z. Chen, S. Han, M. Yan and Z. Lu, *Water, Air, Soil Pollut.*, 2022, **233**, 516.

93 X. Feng, R. Long, C. Liu and X. Liu, *Sep. Purif. Technol.*, 2022, **302**, 122138.
94 S. Vigneshwaran, D. G. Kim and S. O. Ko, *Chemosphere*, 2024, **352**, 141339.
95 W. Zhao, J. H. Cao, J. J. Liao, Y. Liu, X. J. Zeng, J. Y. Shen, X. K. Hong, Y. Guo, H. H. Zeng and Y. Z. Liu, *Rare Met.*, 2024, **43**, 3118–3133.
96 I. Ibrahim, P. P. Falara, E. Sakellis, M. Antoniadou, C. Athanasekou and M. K. Arfanis, *ChemEngineering*, 2024, **8**, 20.
97 M. Liu, P. Ye, M. Wang, L. Wang, C. Wu, J. Xu and Y. Chen, *J. Environ. Chem. Eng.*, 2022, **10**, 108436.
98 X. Zhan, H. Zhang, Y. Zeng, J. Xu, A. Jin, X. Wang, J. Li, Y. Yang and B. Hong, *New J. Chem.*, 2023, **47**, 6958–6966.
99 C. Jin, J. Kang, Z. Li, M. Wang, Z. Wu and Y. Xie, *Appl. Surf. Sci.*, 2020, **514**, 146076.
100 P. S. Selvamani, J. J. Vijaya, L. J. Kennedy, A. Mustafa, M. Bououdina, P. J. Sophia and R. J. Ramalingam, *Ceram. Int.*, 2021, **47**, 4226–4237.
101 T. Xu, S. X. Guan, L. Tang, J. Y. Zhang, C. Luo, H. Wang and N. Zhang, *J. Photochem. Photobiol. A Chem.*, 2023, **441**, 114756.
102 P. Xu, S. Xie, X. Liu, L. Wang, R. Wu and B. Hou, *Chem. Eng. J.*, 2024, **480**, 148233.
103 Y. Song, R. Chen, S. Li, S. Yu, X. Ni, M. Fang and H. Xie, *Nanomaterials*, 2024, **14**, 786.
104 C. Wang, Y. Li, M. Fan, X. Yu, J. Ding, L. Yan, G. Qin, J. Yang and Y. Zhang, *Chem. Eng. J.*, 2024, **479**, 147752.
105 M. Chen, T. Sun, W. Zhao, X. Yang, W. Chang, X. Qian, Q. Yang and Z. Chen, *ACS Omega*, 2021, **6**, 12787–12793.
106 M. Zhao, X. Guo, Z. Meng, Y. Wang, Y. Peng and Z. Ma, *Colloids Surf., A*, 2021, **631**, 127671.
107 E. Jiang, N. Song, G. Che, C. Liu, H. Dong and L. Yang, *Chem. Eng. J.*, 2020, **399**, 125721.
108 M. Govinda Raj, E. Vijayakumar, R. Preetha, M. G. Narendran, B. Neppolian and A. J. Bosco, *J. Alloys Compd.*, 2022, **929**, 167252.
109 J. Jia, L. Zheng, K. Li, Y. Zhang and H. Xie, *Chem. Eng. J.*, 2022, **429**, 132432.
110 J. Ni, Z. Wei, A. Wang, D. Liu, W. Wang, X. Song and Z. Xing, *Environ. Sci.: Nano*, 2023, **10**, 1778–1789.
111 B. Liu, G. Wang, J. Li, B. Liu, R. Li, H. Huang, H. Shi and J. Zhang, *J. Water Process Eng.*, 2024, **63**, 105419.
112 E. Finkelstein, G. M. Rosen and E. J. Rauckman, *Arch. Biochem. Biophys.*, 1980, **200**, 1–16.
113 V. G. Christensen and E. Khan, *Sci. Total Environ.*, 2020, **736**, 139515.
114 A. Serrà, E. Gómez, N. al Hoda al Bast, Y. Zhang, M. Duque, M. J. Esplandiu, J. Esteve, J. Nogués and B. Sepúlveda, *Chem. Eng. J.*, 2024, **487**, 150663.
115 A. Serrà, P. Pip, E. Gómez and L. Philippe, *Appl. Catal., B*, 2020, **268**, 118745.
116 M. Benamara, G. Elvira, R. Dhahri and A. Serrà, *Toxins*, 2021, **13**, 66.
117 H. Wang, X. Li, Q. Ge, Y. Chong and Y. Zhang, *Colloids Surf., B*, 2022, **219**, 112833.
118 J. Liu, W. Cheng, Y. Wang, X. Fan, J. Shen, H. Liu, A. Wang, A. Hui, F. Nichols and S. Chen, *ACS Appl. Nano Mater.*, 2021, **4**, 4361–4370.
119 J. Li, J. Ma and L. Hong, *Nanotechnology*, 2022, **33**, 075706.
120 J. Dai, J. Chen, J. Song, Y. Ji, Y. Qiu, Z. Hong, H. Song, L. Yang, Y. Zhu, L. Li, H. Yang and Z. Hu, *Chem. Eng. J.*, 2021, **421**, 129773.
121 L. Yang, J. Wang, S. Yang, Q. Lu, P. Li and N. Li, *Theranostics*, 2019, **9**, 3992–4005.
122 J. Wang, Z. Li, Y. Yin, H. Liu, G. Tang and Y. Ma, *J. Mater. Sci.*, 2020, **55**, 15263–15274.
123 J. Huang, G. Deng, S. Wang, T. Zhao, Q. Chen, Y. Yang, Y. Yang, J. Zhang, Y. Nan, Z. Liu, K. Cao, Q. Huang and K. Ai, *Adv. Sci.*, 2023, **10**, 2302208.
124 B. Ding, S. Shao, C. Yu, B. Teng, M. Wang and Z. Cheng, *Adv. Mater.*, 2018, **1802479**, 1–10.
125 A. G. Roca, J. F. Lopez-Barbera, A. Lafuente, F. Özel, E. Fantechi, J. Muro-Cruces, M. Hémadi, B. Sepulveda and J. Nogues, *Phys. Rep.*, 2023, **1043**(96), 1–35.
126 W. Kim, S. Lee, D. Seo, D. Kim, K. Kim, E. Kim, J. Kang, K. M. Seong, H. Youn and B. Youn, *Cells*, 2019, **8**, 1–17.
127 J. Soriano, I. Mora-Espí, M. E. Alea-Reyes, L. Pérez-García, L. Barrios, E. Ibáñez and C. Nogués, *Sci. Rep.*, 2017, **7**, 41340.
128 J. Fraxedas, S. García-Gil, S. Monturet, N. Lorente, I. Fernández-Torrente, K. J. Franke, J. I. Pascual, A. Vollmer, R. P. Blum, N. Koch and P. Ordejón, *J. Phys. Chem. C*, 2011, **115**, 18640–18648.
129 S. Stoll and A. Schweiger, *J. Magn. Reson.*, 2006, **178**, 42–55.